Self-sustained Multicentennial Oscillation of the Atlantic Meridional Overturning Circulation in Two-hemisphere Box Models

Xiangying Zhou, Kunpeng Yang, Haijun Yang*

Department of Atmospheric and Oceanic Sciences and Key Laboratory of Polar Atmosphere-ocean-ice System for Weather and Climate of Ministry of Education, Fudan University, Shanghai, 200438, China

Journal of Climate

Submitted

January 6, 2024

Corresponding author: Haijun Yang, yanghj@fudan.edu.cn

ABSTRACT

Our previous studies have established a theory for a self-sustained multicentennial oscillation (MCO) of the Atlantic meridional overturning circulation (AMOC) in a one-hemisphere box model. In this paper, we extend the one-hemisphere model to a more realistic two-hemisphere model, and study the roles of both the thermohaline and wind-driven circulations in the MCO. A similar self-sustained AMOC MCO in the two-hemisphere box model is identified. Several new findings are summarized as follows. First, the salinity advection feedback in the North Atlantic still plays the most important role in controlling AMOC MCO, while that in the South Atlantic is unimportant. Second, in comparison to the self-sustained AMOC MCO in the one-hemisphere box model, the counterpart in the two-hemisphere box model exhibits higher probability of occurrence and less sensitivity to changes in basin geometry. Third, the wind-driven circulation can weaken MCO amplitude because the negative feedback between the wind-driven and thermohaline circulations restrains the salinity advection feedback, while its effect on MCO period is negligible. Fourth, without the thermohaline circulation, there will be no MCO, suggesting the thermohaline circulation is a necessary condition for the AMOC MCO. Similar to previous studies, stochastic freshwater forcing can excite sustained AMOC MCO, and the MCO is an intrinsic mode of the thermohaline circulation. We also find a damped millennial oscillatory mode in the two-hemispheric box model, which needs to be investigated further in the future.

KEYWORDS: Atlantic meridional overturning circulation, Box model, Self-sustained multicentennial oscillation, Thermohaline circulation, Wind-driven circulation

1. Introduction

Through analyses of proxy data and model simulation outputs, researchers have identified multicentennial climate variability (Wanner et al. 2008; Moffa- Sánchez et al. 2019; Askjær et al. 2022), which may have influenced the course of human history to some extent. It is widely recognized that the low-frequency climate variability beyond decadal timescale is linked to ocean circulations, particularly the Atlantic meridional overturning circulation (AMOC) (Stocker and Mysak 1992; Srokosz et al. 2012). This association is supported by significant signals of multicentennial variability observed in proxy data within the North Atlantic region (Sejrup et al. 2011; Moffa- Sánchez et al. 2019; Askjær et al. 2022). Moreover, numerous model simulations have consistently indicated the existence of multicentennial variability of the AMOC (e.g., Park and Latif 2008; Delworth and Zeng 2012; Martin et al. 2013, 2015; Jiang et al. 2021; Meccia et al. 2022; Mehling et al. 2023), which may induce multicentennial variability of the Earth's climate system.

Some studies suggested that the multicentennial variability of the AMOC is driven by external natural forcing of the climate system (e.g., Weber et al. 2004), while others focused on internal processes within the ocean itself (e.g., Winton and Sarachik 1993; te Raa and Dijkstra 2003; Delworth and Zeng 2012; Cao et al. 2023). In the studies supporting this variability arose from an internal process, most researchers agreed that salinity anomalies in the North Atlantic deep-water (NADW) formation region is a controlling factor (e.g., Mysak et al. 1993; Sévellec et al. 2006; Delworth and Zeng 2012; Cao et al. 2023). However, there is an ongoing debate regarding where the salinity anomaly came from and how it interacted with the NADW formation, thereby generating the multicentennial variability of the AMOC. Some studies associated this variability with the Arctic Ocean and proposed that southward salinity anomalies from the Arctic Ocean to the North Atlantic drive the multicentennial variation (Jiang et al. 2021; Meccia et al. 2022; Mehling et al. 2023), despite their different perspectives on the generation of the salinity anomalies in the Arctic Ocean. Another perspective asserts that the most influential factor for the multicentennial variability of the AMOC is the seawater originated from the southern region, including regions such as the equator, South Atlantic, and Southern Ocean (Park and Latif 2008; Delworth and Zeng 2012; Martin et al. 2013, 2015). Recently, Prange et al. (2023) identified the multicentennial variability of the AMOC in CESM1.2 under boundary conditions of the Last Glacial Maximum (LGM) when no significant changes in external forcing were observed. Their findings suggested that this variability and salinity anomaly in the NADW formation region are driven by the transport of the Antarctic intermediate water (AAIW). Overall, the diverse viewpoints on the driving mechanisms behind the multicentennial variability of the AMOC stress the need for fundamental understanding of its origin.

Specific processes responsible for generating and maintaining the multicentennial variability of the AMOC can be more cleanly investigated in simple theoretical models. Recently, Li and Yang (2022) (hereafter LY22) identified a multicentennial eigenmode of the AMOC in a one-hemisphere box model including only saline processes, which can exhibit self-sustained multicentennial oscillation (MCO) in the presence of enhanced vertical mixing in the NADW formation region. Yang et al. (2023) (hereafter YYL23) expanded the work of LY22 by incorporating both thermal and saline processes in their one-hemisphere box model. Their findings indicated that the thermal processes can stabilize the oscillatory system and shorten the oscillation period; however, the fundamental behavior of the oscillation system is still controlled by the saline processes. They found that besides the internal nonlinear vertical mixing (LY22), the self-sustained AMOC MCO can also be maintained by a weak nonlinear relationship between AMOC strength and meridional density gradient.

This study is a subsequent investigation in our ongoing series of theoretical studies on the AMOC MCO. In this work, we expand the one-hemisphere box model developed in LY22 and YYL23 to a two-hemisphere box model. Additionally, we incorporate both the thermohaline and wind-driven components of the AMOC, allowing for a comprehensive examination of the influence of the wind-driven circulation on the low-frequency variability of the AMOC. While previous research demonstrated the significance of the wind-driven circulation in influencing the AMOC (Pasquero and Tziperman 2004; Guan and Huang 2008; Yong-Qi and Lei 2008; Klockmann et al. 2020; Sun et al. 2021), its specific role in the AMOC MCO remains an area of further investigation. Therefore, the primary objective of this paper is to address a research gap by conducting an in-depth analysis of the impact of the wind-driven circulation on the AMOC MCO.

Results in this paper show that the multicentennial eigenmode and AMOC MCO also exist in the two-hemisphere box model, which are less affected by the model parameters compared to those in the one-hemisphere box model. Adding antisymmetric transports from the equator to polar oceans in the two-hemisphere box model, i.e., including the effect of the wind-driven circulations, can stabilize the oscillation, reduce the oscillatory amplitude, and prolong the oscillatory period slightly. In this paper, we depict the inter-hemispheric nature of the AMOC more realistically, enhancing our understanding of AMOC MCO and enriching the theory beyond the limitations of the single-hemisphere model and the thermohaline circulation. This paper is organized as follows. In section 2, a two-hemisphere box model with only salinity equations (hereafter the 6S model) is introduced, and eigenvalues of this linear system are analyzed. In section 3, we realize a self-sustained AMOC MCO in the 6S model and investigate the role of the subpolar South Atlantic. In section 4, temperature equations and wind-driven circulation are incorporated, and their effects on the AMOC MCO are analyzed. In section 5, we investigate stochastically forced oscillations in the box model. Summary and discussion are presented in section 6. Pertinent background information obtained from two coupled models, and the derivation of theoretical formulas for several simplified two-hemisphere models are included in appendices.

2. Two-hemisphere box model

a. Salinity-only thermohaline model

The two-hemisphere box model used here consists of six ocean boxes (Fig. 1). With a zonal width of 5200 km and a meridional extent of 140°, the model domain spans two hemispheres and is separated into three zones by latitudes 45°N and 30°S. The AMOC is clockwise in the box model, sinking in the subpolar North Atlantic and rising in the subpolar South Atlantic.

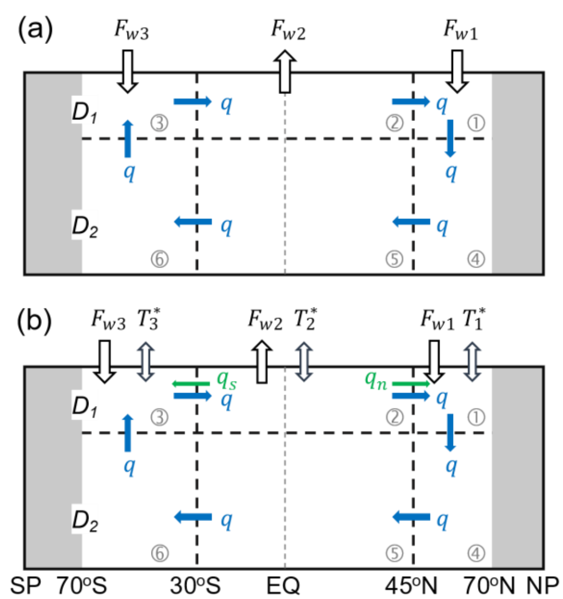

FIG. 1. Schematic diagrams of ocean box models. (a) The 6-box salinity-only model (6S model); and (b) the 6-box temperature-salinity model (6TS model) with the wind-driven circulation included. The circled numbers (e.g., ① and ②) denote the ocean boxes. Boxes 1 and 4 represent the upper and lower subpolar North Atlantic, respectively; boxes 2 and 5 represent the upper and lower tropical oceans, respectively; boxes 3 and 6 represent the upper and lower subpolar South Atlantic, respectively. D_1 and D_2 are the depths of the upper and lower oceans, respectively. F_{w1}, F_{w2}, and F_{w3} are the virtual salt fluxes into boxes 1-3, representing surface freshwater fluxes in

reality. T_1^*, T_2^*, and T_3^* are the restoring temperatures of boxes 1-3. q represents the AMOC. q_n and q_s are northward and southward transports by the wind-driven circulation, respectively.

The salinity equations in the 6S model (Fig. 1a) can be written as follows,

$$V_1\dot{S_1} = q(S_2 - S_1) + F_{w1} \tag{1a}$$

$$V_2\dot{S_2} = q(S_3 - S_2) + F_{w2} \tag{1b}$$

$$V_3\dot{S_3} = q(S_6 - S_3) + F_{w3} \tag{1c}$$

$$V_4\dot{S_4} = q(S_1 - S_4) \tag{1d}$$

$$V_5\dot{S_5} = q(S_4 - S_5) \tag{1e}$$

$$V_6\dot{S_6} = q(S_5 - S_6) \tag{1f}$$

where V_i and S_i are the volume and salinity of box i, and q is the AMOC strength. F_{wi} is the virtual salt flux for the upper boxes, representing surface freshwater fluxes across corresponding boxes.

The equilibrium solutions of Eq. (1) are,

$$\bar{q}(\overline{S_1} - \overline{S_2}) = F_{w1} \tag{2a}$$

$$\bar{q}(\overline{S_2} - \overline{S_3}) = F_{w2} \tag{2b}$$

$$\bar{q}(\overline{S_3} - \overline{S_1}) = F_{w3} \tag{2c}$$

$$\overline{S_1} = \overline{S_4} = \overline{S_5} = \overline{S_6} \tag{2d}$$

$$F_{w1} + F_{w2} + F_{w3} = 0 \tag{2e}$$

where, $\bar{q}$ is set to 24 Sv. F_{w1}, F_{w2}, and F_{w3} are set to -7.2×10^7, 7.44×10^7, and -0.24×10^7 psu m^3 s^{-1}, which give $\overline{S_1} = 33.9$, $\overline{S_2} = 36.9$, and $\overline{S_3} = 33.8$ psu, respectively. The model is tuned so that its equilibria nearly agree with the results of the two coupled models examined in Appendix A. Other parameters used in the 6S model are listed in Table 1.

TABLE 1. Standard values of parameters and equilibria used in this study. WDC is an abbreviation of wind-driven circulation.

Symbol	Physical meaning	Value with units
L_1, L_2, L_3, L	Meridional scales of northern subpolar, tropical, southern	25°, 75°, 40°, 140°

	subpolar ocean boxes, and the total scale	
D_1, D_2, D	Thicknesses of the upper, deeper, and their sum	1000, 3000, 4000 m
V_1	Volume of box 1	1.443×10^{16} m^3 (5200 km wide)
V_2, V_3, V_4, V_5, V_6	Volumes of boxes 2, 3, 4, 5, and 6	$3V_1$, $1.6V_1$, $3V_1$, $9V_1$, $4.8V_1$
γ	Restoring coefficient of boxes 1, 2, and 3	3.171×10^{-8} s^{-1}
T_1^*, T_2^*, T_3^*	Restoring temperatures of boxes 1, 2, and 3	3.7, 24.5, 7.7 ℃ (without WDC)
		3.4, 24.6, 7.8 ℃ (with WDC)
F_{w1}, F_{w2}, F_{w3}	Surface virtual salt fluxes into boxes 1, 2, and 3	-7.2×10^7, 7.44×10^7, -0.24×10^7 psu m^3 s^{-1} (without WDC)
		-8.97×10^7, 7.63×10^7, 1.34×10^7 psu m^3 s^{-1} (with WDC)
$\bar{q}$	Mean strength of the AMOC	24 Sv (10^6 m^3 s^{-1})
λ	Linear closure coefficient	21.3 Sv kg^{-1} m^3
α	Thermal expansion coefficient	1.468×10^{-4} ℃$^{-1}$
β	Saline contraction coefficient	7.61×10^{-4} psu^{-1}
ρ_0	Reference seawater density	1.0×10^3 kg m^{-3}
$\overline{q_n}$, $\overline{q_s}$	Mean transports by the WDC	5.9, 5.1 Sv
k_n, k_s	Wind-driven advection coefficients for the NA and SA	0.307 Sv ℃$^{-1}$
$\overline{T_1}$, $\overline{T_2}$, $\overline{T_3}$, $\overline{T_4}$, $\overline{T_5}$, $\overline{T_6}$	Equilibrium temperatures of six boxes	4.9, 24.2, 7.2, 4.9, 4.9, 4.9 ℃
$\overline{S_1}$, $\overline{S_2}$, $\overline{S_3}$, $\overline{S_4}$, $\overline{S_5}$, $\overline{S_6}$	Equilibrium salinities of six boxes	33.9, 36.9, 33.8, 33.9, 33.9, 33.9 psu

Eq. (1) can be linearized as follows,

$$V_1\dot{S}_1' = \bar{q}(S_2' - S_1') + q'(\overline{S_2} - \overline{S_1}) \tag{3a}$$

$$V_2\dot{S}_2' = \bar{q}(S_3' - S_2') + q'(\overline{S_3} - \overline{S_2}) \tag{3b}$$

$$V_3\dot{S}_3' = \bar{q}(S_6' - S_3') + q'(\overline{S_6} - \overline{S_3}) \tag{3c}$$

$$V_4\dot{S}_4' = \bar{q}(S_1' - S_4') \tag{3d}$$

$$V_5\dot{S}_5' = \bar{q}(S_4' - S_5') \tag{3e}$$

$$V_6\dot{S}_6' = \bar{q}(S_5' - S_6') \tag{3f}$$

In Eq. (3), the AMOC anomaly q' is parameterized as a linear function of density difference between two subpolar boxes, capturing the promotive role of the NADW and the counteractive role of the Antarctic Bottom Water (AABW) in influencing the AMOC (Kamenkovich and Goodman 2000; Swingedouw et al. 2009). This linear relation is validated in two coupled models (CESM1.0 and EC-Earth3-Veg-LR; Appendix A, Figs. A1, A2), and can be expressed as follows,

$$q = \bar{q} + q' = \bar{q} + \lambda \Delta\rho' \tag{4}$$

$$\Delta\rho' = \rho_0\beta[\delta(S_1' - S_3') + (1 - \delta)(S_4' - S_6')]$$

and

$$\delta = \frac{V_1}{V_1 + V_4} = \frac{V_3}{V_3 + V_6} = \frac{D_1}{D} \tag{5}$$

b. Linear stability analysis

Eigenvalues of the 6S model can be obtained numerically. Using the parameters in Table 1, we obtain two pairs of conjugate eigenvalues, corresponding to a multicentennial (ω = 0.34 ± 5.85i) and a millennial oscillatory mode (ω = 8.34 ± 1.12i) (Table 2), respectively. The system has two additional eigenvalues: 0 and –19.19, corresponding to a zero mode (i.e., the equilibrium climate) and a purely damped mode with an e-folding time of about 20 years.

The multicentennial mode has a period of about 340 years and an e-folding time of about 920 years, indicating a weakly unstable oscillation. The multicentennial mode depends closely on the closure parameter λ (Fig. 2). The real part of the eigenvalue [Re(ω)] increases with λ (Fig. 2a), while the imaginary part [Im(ω)] has a maximum value when λ = 21.3 Sv kg^{-1} m^3 (Fig. 2b). This dependence is similar to that in the one-hemisphere box model of LY22 and YYL23. Eigenvalues under $\lambda < 0$ (Fig. 2, dashed curves) do not have any physical meaning and are plotted in Fig. 2 only for mathematical completeness.

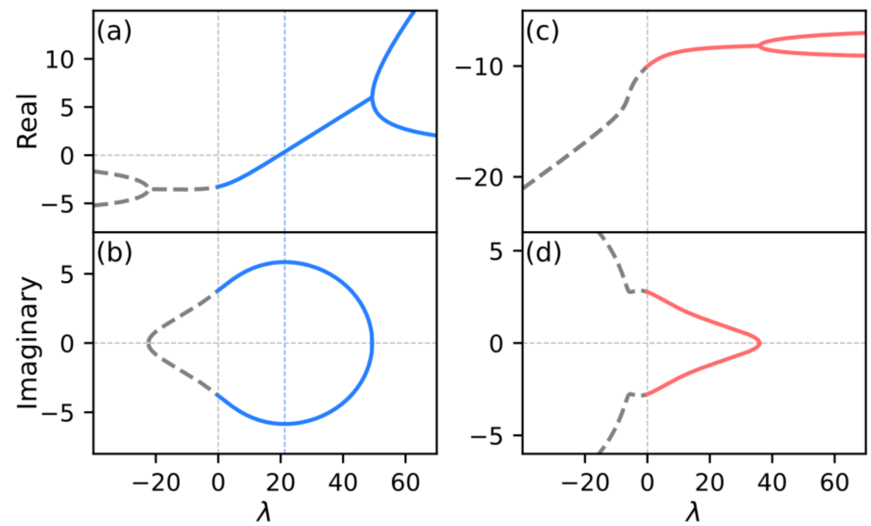

FIG. 2. Dependences of (a) Re(ω) and (b) Im(ω) of the multicentennial oscillatory modes on λ (units: Sv kg^{-1} m^3) in the 6S model using the parameters in Table 1. Solid curves are for $\lambda > 0$; dashed gray curves are for $\lambda \le 0$ and have no physical meaning. The vertical dashed blue line corresponds to λ = 21.3 Sv kg^{-1} m^3. The units of the ordinate are 10^{-10} s^{-1}. (c) and (d) are the same as (a) and (b), but for millennial oscillatory modes in the 6S model.

The millennial oscillatory mode has a period about 1800 years and a much shorter e-folding time of about –40 years, which is unique here and absent in the one-hemispheric model. With the increase of λ, Im(ω) decreases and Re(ω) increases roughly monotonically (Figs. 2c, d). However, Re(ω) is always negative and much smaller than Im(ω), suggesting that this millennial mode is a strongly damped mode.

3. Robust multicentennial oscillations

a. Self-sustained oscillations

In studies employing theoretical models, sustained oscillations can arise from either external forcing or intrinsic nonlinearity (Griffies and Tziperman 1995; Rivin and Tziperman 1997; LY22; YYL23). A self-sustained AMOC oscillation can be excited by enhanced vertical mixing in the subpolar North Atlantic (LY22), or by introducing a nonlinear relationship between the AMOC strength and meridional density difference (Rivin and Tziperman 1997; YYL23). Here, we simply adopt the approach in LY22.

Adding enhanced vertical mixing between the upper and lower subpolar oceans (boxes 1 and 4) in the 6S model, Eqs. (3a) and (3d) become,

$$V_1\dot{S}_1' = \bar{q}(S_2' - S_1') + q'(\overline{S_2} - \overline{S_1}) - k_m(S_1' - S_4') \tag{6a}$$

$$V_4\dot{S}_4' = \bar{q}(S_1' - S_4') + k_m(S_1' - S_4') \tag{6b}$$

$$k_m = \kappa {q'}^2 \tag{6c}$$

where κ is a positive constant and is set to 10^{-3} m^{-3} s in this paper. As a result, k_m is always positive and represents a process that always transfers the salinity anomaly of upper ocean downward to lower ocean, no matter whether the AMOC is stronger or weaker than usual. The physics of the enhanced subpolar vertical mixing process was discussed in detail in LY22.

Figure 3 shows the results through numerical integration of the 6S model [Eq. (3)], and the results when enhanced vertical mixing is introduced in the subpolar North Atlantic [Eqs. (3) and (6)]. The integration starts from an initial salinity perturbation in the subpolar North Atlantic (S_1' = –0.02 psu). The forward fourth-order Runge-Kutta method is used to solve the equations. The integration time step is one year; the total integration length is longer than 10000 years. Given the velocity closure parameter λ = 21.3 Sv kg^{-1} m^3, the time series of salinity anomalies show oscillations with periods about 340 years and gradually enhancing amplitude (dashed curves in Fig. 3a), which are predicted by the eigenvalues discussed in section 2. After adding the enhanced mixing in the subpolar North Atlantic, the unstable oscillation becomes a self-sustained oscillation with a limited amplitude (solid curves in Fig. 3a).

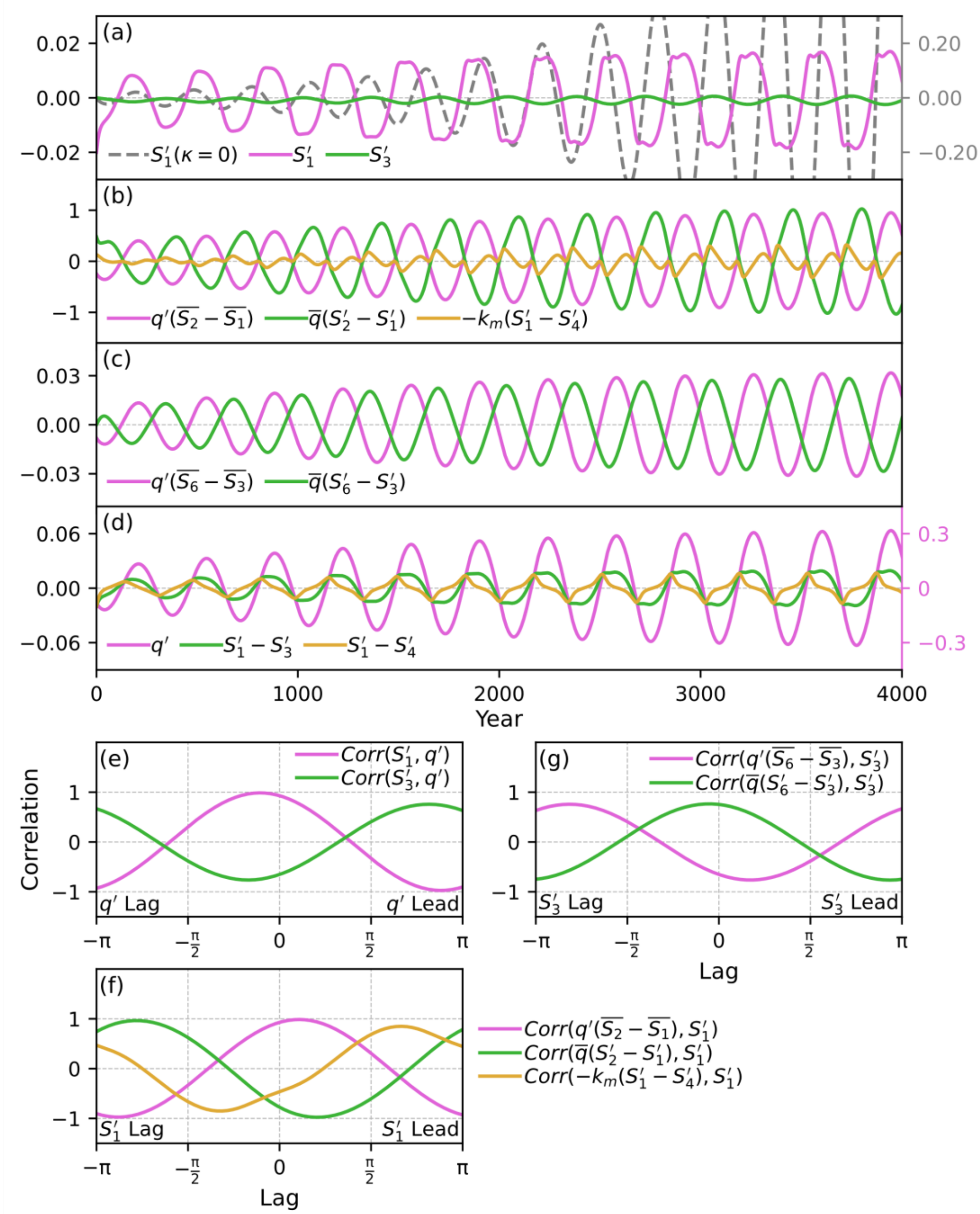

FIG. 3. (a) Unstable oscillation of S_1' (dashed curve; units: psu) in the 6S model without enhanced vertical mixing ($\kappa = 0$) in the subpolar North Atlantic; self-sustained oscillations of S_1' and S_3' with the enhanced vertical mixing. (b)-(c) Self-sustained oscillations of salinity terms (units: Sv psu) in the 6S model with the enhanced vertical mixing in the subpolar North Atlantic: (b) $q'(\overline{S_2}-\overline{S_1})$, $\overline{q}(S_2'-S_1')$, and $-k_m(S_1'-S_4')$, which are on the right-hand side of Eq. (6a), (c) $q'(\overline{S_1}-\overline{S_3})$ and $\overline{q}(S_6'-S_3')$, which are on the right-hand side of Eq. (3c). (d) Time series of q' (units: Sv), $S_1'-S_3'$, and $S_1'-S_4'$. (e) Lead-lag correlation coefficients of q' with S_1' and S_3'. For negative lags, salinity anomaly leads. (f) Lead-lag correlation coefficients between S_1' and individual salinity terms on the right-hand side of Eq. (6a), which are $q'(\overline{S_2}-\overline{S_1})$, $\overline{q}(S_2'-S_1')$, and $-k_m(S_1'-S_4')$. Salinity terms lead for negative lags, salinity terms lead. (g) Lead-lag correlation coefficients between S_3' and individual salinity terms on the right-hand side of Eq. (3c), which are $q'(\overline{S_1}-\overline{S_3})$ and $\overline{q}(S_6'-S_3')$. For negative lags, salinity terms lead. Legends for the curves are labeled on the respective panels.

Physical processes contributing to the AMOC MCO are examined here. q' is roughly in phase with S_1' and out of phase with S_3' (Fig. 3e); thus, q' synchronizes with $S_1' - S_3'$ (Fig. 3d). Compared to S_3', S_1' has a larger amplitude and dominates q'. The growth of S_1' depends on three processes, as shown in Eq. (6a). The perturbation advection $q'(\overline{S_2} - \overline{S_1})$ has a positive correlation with S_1', which leads to positive feedback between S_1' and q'. The mean advection [$\overline{q}(S_2' - S_1')$] and enhanced vertical mixing [$-k_m(S_1' - S_4')$] lead to negative feedback for q' because S_1' is negatively correlated to the change of itself. The lead-lag correlation in Fig. 3f clearly illustrates the feedbacks of these terms with S_1'. Supposing that there is a positive anomaly in q' initially, the positive perturbation advection [$q'(\overline{S_2} - \overline{S_1})$] first contributes to the growth of S_1' and further increases q'. Then, the growing S_1' enhances the negative feedback through strengthening mean advection [$\overline{q}(S_2' - S_1')$] and vertical mixing [$-k_m(S_1' - S_4')$], which in turn restricts the growth of S_1' and ocean stratification ($S_1' - S_4'$) (Fig. 3d). As a result, the further growth of q' is restrained and the oscillation is stabilized. These processes were deliberated in our previous studies using the one-hemisphere box model (LY22; YYL23).

The subpolar South Atlantic plays the secondary role in adjusting the AMCO MCO because of the smaller amplitude of S_3' (Fig. 3a). For S_3', both the perturbation advection [$q'(\overline{S_6} - \overline{S_3})$] and mean advection [$\overline{q}(S_6' - S_3')$] in Eq. (3c) give negative feedbacks (Fig. 3g). However, for q', these two processes play as negative feedback and positive feedback, respectively. Starting with a positive perturbation of q', the perturbation advection [$q'(\overline{S_6} - \overline{S_3})$] contributes to the growth of S_3' (Fig. 3f), which tends to reduce q' (Fig. 3e). Physically, it can be understood as that positive $q'(\overline{S_6} - \overline{S_3})$ removes the freshwater from the subpolar South Atlantic. As a result, the AABW formation is enhanced, which can restrain the AMOC development in the North Atlantic eventually. Also, growing S_3' leads to the decline of mean advection [$\overline{q}(S_6' - S_3')$] (Fig. 3g), which in turn restricts the growth of S_3' but promotes q'. Since q' is mainly controlled by ($S_1' - S_3'$) [Eq. (5)], the smaller amplitude of S_3' than that of S_1' (Fig. 3a) suggests a minor role of the Southern Ocean in the AMOC MCO.

b. Sensitivity of MCO mode to basin geometry

The model basin geometry can affect both the e-folding time and period of the AMOC MCO (Fig. 4). Keeping $\overline{q}$, $\overline{F_w}$, V, and λ unchanged as in Table 1, the dependence of the multicentennial eigenmode on the volumes of the subpolar North Atlantic ($V_1 + V_4$) and the global upper ocean ($V_1 +$

$V_2 + V_3$) is exhibited in Figs. 4a, b. The influence of the volume of the subpolar South Atlantic ($V_3 + V_6$) on the multicentennial mode is analyzed in Figs. 4c, d. The blue star denotes the mode under the standard parameters in Table 1. Similar to Fig. 9 in LY22, the stability thresholds of the 6S and 5S models (Appendix B, Fig. B1) are marked by the pink and purple curves, respectively, which divide the phase space into three regions with different stability: the oscillations are decayed in region 1, self-sustained in region 2 when including enhanced vertical mixing, and unstable in region 3 regardless of the presence of enhanced vertical mixing or not.

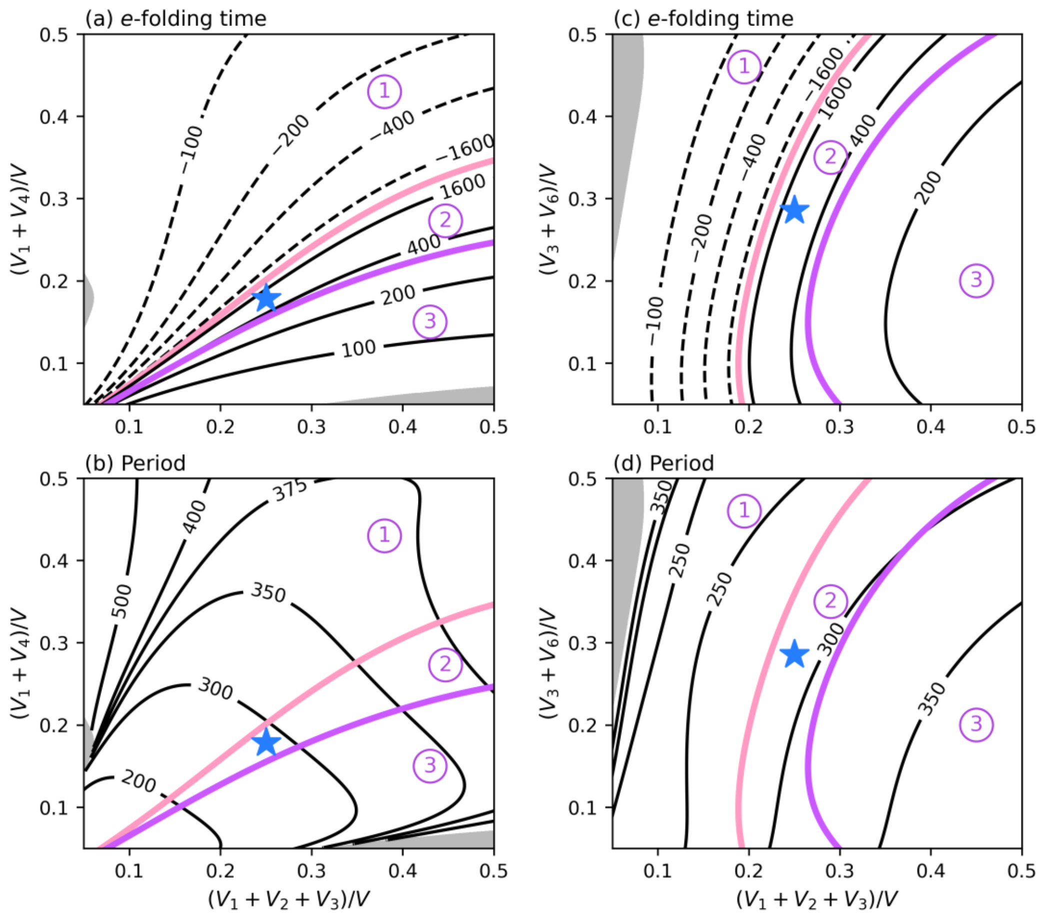

FIG. 4. Sensitivity of (a) period (units: year) and (b) e-folding time (units: year) of multicentennial oscillatory modes to model geometry in the 6S model. The abscissa and ordinate represent the volume fractions of the upper ocean $(V_1 + V_2 + V_3)/V$ and the northern subpolar ocean $(V_1 + V_4)/V$, respectively, where V is the total ocean volume. The solid pink and purple curves are the stability thresholds of the 6S and 5S models, respectively, dividing the contour plots into three regions. The oscillatory modes are decayed in region 1, self-sustained in region 2, and unstable in region 3 when considering enhanced vertical mixing. The blue star denotes the standard geometry and eigenmode using the parameters listed in Table 1. The values of the other parameters are the same as those listed in Table 1. Gray regions represent the ratios of e-folding time to period larger than 0.1. (c) and (d) are the same as (a) and (b), except that the ordinates represent the volume fraction of the subpolar ocean in the Southern Hemisphere $(V_3 + V_6)/V$.

Let us focus on the self-sustained modes in region 2 next. In the 6S model, the multicentennial timescale has a higher probability to occur, varying from 200 to 400 years in this phase space (Figs. 4b, d), in despite of the volume changes of the upper ocean ($V_1 + V_2 + V_3$), subpolar North Atlantic ($V_1 + V_4$), and subpolar South Atlantic ($V_3 + V_6$). In particular, the volume of the subpolar South Atlantic has much smaller effect on the period of the AMOC MCO (Fig. 4d). In contrast, the stability of the self-sustained oscillations is quite sensitive to the volume changes of the upper ocean and subpolar North Atlantic (Figs. 4a, c). With the increasing volume of the upper ocean ($V_1 + V_2 + V_3$), the e-folding time of the eigenmode decreases significantly (from 1600 to 400 years), suggesting that the oscillation modes can be converted from a weak unstable mode to a strong unstable mode in the absence of enhance vertical mixing (Figs. 4a, c). On the contrary, with the increasing volume of the subpolar North Atlantic ($V_1 + V_4$), the e-folding time of the eigenmode increases significantly from 400 to 1600 years, suggesting a trend of being a stabilizing oscillation. However, the e-folding time of the eigenmode is less sensitive to the volume of the subpolar South Atlantic ($V_3 + V_6$) (Fig. 4c), suggesting that the South Atlantic has a weak effect on the AMOC MCO. This result is qualitatively consistent our conclusion drawn in section 3a that the Southern Ocean has a minor impact on the AMOC MCO. This finding also agrees with the results of the one-hemisphere box model in LY22, in which only the role of subpolar North Atlantic is highlighted in the AMOC MCO.

4. Two-hemisphere box model with wind-driven circulation

To consider wind-driven circulation in our box model, we need temperature equations, since the strength of such wind-driven circulation is roughly determined by the meridional temperature gradient (Vallis and Farneti 2009). In fact, the meridional overturning circulation includes both thermohaline and wind-driven components. In the Atlantic, the thermohaline component is much more important than the wind-driven component; the AMOC is usually represented by its thermohaline component. However, in the Pacific there are strong wind-driven circulations while the thermohaline circulation is absent; the wind-driven circulations, which are referred to as the subtropical cells, exist mainly in the tropics and have an antisymmetric structure with respect to the equator (McCreary and Lu 1994; Schott et al. 2004).

The box model discussed in this section includes both temperature and salinity equations (termed as the 6TS model), in which both the wind-driven and thermohaline circulations are parameterized (Fig. 1b). Equations of the 6TS model with the wind-driven circulation are written as follows,

$$V_1\dot{T}_1 = q(T_2 - T_1) + V_1\gamma(T_1^* - T_1) + q_n(T_2 - T_1) \tag{7a}$$

$$V_2\dot{T}_2 = q(T_3 - T_2) + V_2\gamma(T_2^* - T_2) - q_n(T_2 - T_1) - q_s(T_2 - T_3) \tag{7b}$$

$$V_3\dot{T}_3 = q(T_6 - T_3) + V_3\gamma(T_3^* - T_3) + q_s(T_2 - T_3) \tag{7c}$$

$$V_4\dot{T}_4 = q(T_1 - T_4) \tag{7d}$$

$$V_5\dot{T}_5 = q(T_4 - T_5) \tag{7e}$$

$$V_6\dot{T}_6 = q(T_5 - T_6) \tag{7f}$$

$$V_1\dot{S}_1 = q(S_2 - S_1) + F_{w1} + q_n(S_2 - S_1) \tag{7g}$$

$$V_2\dot{S}_2 = q(S_3 - S_2) + F_{w2} - q_n(S_2 - S_1) - q_s(S_2 - S_3) \tag{7h}$$

$$V_3\dot{S}_3 = q(S_6 - S_3) + F_{w3} + q_s(S_2 - S_3) \tag{7i}$$

$$V_4\dot{S}_4 = q(S_1 - S_4) \tag{7j}$$

$$V_5\dot{S}_5 = q(S_4 - S_5) \tag{7k}$$

$$V_6\dot{S}_6 = q(S_5 - S_6) \tag{7l}$$

A restoring boundary condition for surface temperature is employed in (7a-c), with γ being the restoring coefficient and set to 3.171×10^{-8} s^{-1} (corresponding to a 1-year restoring timescale). T_1^*, T_2^*, and T_3^* are the restoring temperatures for boxes 1, 2, and 3, respectively. q refers to the mass transport by the thermohaline circulation. q_n and q_s (units: Sv) refer to the mass transports by the northern and southern branches of the wind-driven circulation, respectively. For the convenience of discussion, we use 6TS_THC+WDC for the 6TS model considering both the thermohaline and wind-driven circulations; similarly, we use 6TS_THC (6TS_WDC) to represent the model considering only the thermohaline (wind-driven) circulation.

The equilibrium states of the 6TS model can be written as follows,

$$\bar{q}(\bar{T}_2 - \bar{T}_1) + V_1\gamma(T_1^* - \bar{T}_1) + \overline{q_n}(\bar{T}_2 - \bar{T}_1) = 0 \tag{8a}$$

$$\bar{q}(\bar{T}_3 - \bar{T}_2) + V_2\gamma(T_2^* - \bar{T}_2) - \overline{q_n}(\bar{T}_2 - \bar{T}_1) - \bar{q}_s(\bar{T}_2 - \bar{T}_3) = 0 \tag{8b}$$

$$\bar{q}(\bar{T}_6 - \bar{T}_3) + V_3\gamma(T_3^* - \bar{T}_3) + \bar{q}_s(\bar{T}_2 - \bar{T}_3) = 0 \tag{8c}$$

$$\bar{T}_1 = \bar{T}_4 = \bar{T}_5 = \bar{T}_6 \tag{8d}$$

$$\bar{q}(\bar{S}_1 - \bar{S}_2) + \overline{q_n}(\bar{S}_1 - \bar{S}_2) = F_{w1} \tag{8e}$$

$$\bar{q}(\bar{S}_2 - \bar{S}_3) + \overline{q_n}(\bar{S}_2 - \bar{S}_1) + \bar{q}_s(\bar{S}_2 - \bar{S}_3) = F_{w2} \tag{8f}$$

$$\bar{q}(\bar{S}_3 - \bar{S}_6) + \bar{q}_s(\bar{S}_3 - \bar{S}_2) = F_{w3} \tag{8g}$$

$$\bar{S}_1 = \bar{S}_4 = \bar{S}_5 = \bar{S}_6 \tag{8h}$$

$$F_{w1} + F_{w2} + F_{w3} = 0 \tag{8i}$$

Here, different boundary conditions are used for cases with and without the wind-driven circulation (Table 1). For the 6TS_THC model without the wind-driven circulation, $\overline{q_n} = \overline{q_s} = 0$, T_1^*, T_2^*, and T_3^* are set to 3.7, 24.5, and 7.7 °C, respectively. For the 6TS_THC+WDC model, $\overline{q_n}$ and $\overline{q_s}$ are not zero, F_{w1}, F_{w2}, and F_{w3} are set to –8.97×10^7, 7.63×10^7, and 1.34×10^7 psu m^3 s^{-1}, and T_1^*, T_2^*, and T_3^* are set to 3.4, 24.6, and 7.8 °C, respectively, to keep the equilibrium salinities and temperatures identical to those in the 6TS_THC model. In this paper, we assume $\bar{q}$ and $\overline{q_n}$ ($\overline{q_s}$) are positive, representing the clockwise climatological thermohaline circulation in the Atlantic, and mean northward (southward) transport in the Northern (Southern) Hemisphere, respectively. $\overline{q_n}$ ($\overline{q_s}$) always transports heat poleward because the upper-ocean water moving poleward is always warmer than the lower-ocean water moving equatorward.

The linearized equations of the 6TS model are given below,

$$V_1\dot{T}_1' = \bar{q}(T_2' - T_1') + q'(\overline{T}_2 - \overline{T}_1) - V_1\gamma T_1' + \overline{q_n}(T_2' - T_1') + q_n'(\overline{T}_2 - \overline{T}_1) \tag{9a}$$

$$V_2\dot{T}_2' = \bar{q}(T_3' - T_2') + q'(\overline{T}_3 - \overline{T}_2) - V_2\gamma T_2' - \overline{q_n}(T_2' - T_1') - q_n'(\overline{T}_2 - \overline{T}_1) - \overline{q_s}(T_2' - T_3') - q_s'(\overline{T}_2 - \overline{T}_3) \tag{9b}$$

$$V_3\dot{T}_3' = \bar{q}(T_6' - T_3') + q'(\overline{T}_6 - \overline{T}_3) - V_3\gamma T_3' + \overline{q_s}(T_2' - T_3') + q_s'(\overline{T}_2 - \overline{T}_3) \tag{9c}$$

$$V_4\dot{T}_4' = \bar{q}(T_1' - T_4') \tag{9d}$$

$$V_5\dot{T}_5' = \bar{q}(T_4' - T_5') \tag{9e}$$

$$V_6\dot{T}_6' = \bar{q}(T_5' - T_6') \tag{9f}$$

$$V_1\dot{S}_1' = \bar{q}(S_2' - S_1') + q'(\overline{S}_2 - \overline{S}_1) + \overline{q_n}(S_2' - S_1') + q_n'(\overline{S}_2 - \overline{S}_1) \tag{9g}$$

$$V_2\dot{S}_2' = \bar{q}(S_3' - S_2') + q'(\overline{S}_3 - \overline{S}_2) - \overline{q_n}(S_2' - S_1') - q_n'(\overline{S}_2 - \overline{S}_1) - \overline{q_s}(S_2' - S_3') - q_s'(\overline{S}_2 - \overline{S}_3) \tag{9h}$$

$$V_3\dot{S}_3' = \bar{q}(S_6' - S_3') + q'(\overline{S}_6 - \overline{S}_3) + \overline{q_s}(S_2' - S_3') + q_s'(\overline{S}_2 - \overline{S}_3) \tag{9i}$$

$$V_4\dot{S}_4' = \bar{q}(S_1' - S_4') \tag{9j}$$

$$V_5\dot{S}_5' = \bar{q}(S_4' - S_5') \tag{9k}$$

$$V_6\dot{S}_6' = \bar{q}(S_5' - S_6') \tag{9l}$$

where q' is determined by both temperature and salinity anomalies,

$$q' = q_T' + q_S' = \lambda(\Delta\rho_T' + \Delta\rho_S') \tag{10a}$$

$$\Delta\rho_T' = -\rho_0\alpha[\delta(T_1' - T_3') + (1-\delta)(T_4' - T_6')] \tag{10b}$$

$$\Delta\rho_S' = \rho_0\beta[\delta(S_1' - S_3') + (1-\delta)(S_4' - S_6')] \tag{10c}$$

The forms of q_n' and q_s' are derived from the assumption made by Vallis and Farneti (2009), where the heat transport is given by the product of gyre mass fluxes with a temperature difference multiplied by heat capacity. If the volume transport of the wind-driven circulation is given by the Sverdrup balance, the meridional heat transport can be scaled roughly by using,

$$OHT_{wdc} \sim \frac{\tau^x L_x}{\beta L_y} c\Delta\theta_o \tag{11}$$

where τ^x is the zonal surface wind stress, L_x is the zonal extent of the basin, L_y is the meridional scale of the gyre, c is the heat capacity of seawater per unit mass, β is the meridional gradient of the Coriolis parameter, and $\Delta\theta_o$ is the temperature difference between poleward and equatorward flowing waters, an upper bound of the estimate for the meridional temperature difference across the subtropical gyre. In other words, OHT_{wdc} is proportional to the zonal wind and meridional temperature difference. Thus, the wind-driven circulation strength can be approximated to be proportional to τ^x, which is, in turn, roughly proportional to the meridional temperature difference based on the thermal wind relation. Therefore, the wind-driven volume transports q_n and q_s can be parameterized as follows,

$$q_n = \overline{q_n} + q_n' = \kappa_n(\overline{T}_2 - \overline{T}_1) + \kappa_n(T_2' - T_1') \tag{12a}$$
$$q_s = \overline{q_s} + q_s' = \kappa_s(\overline{T}_2 - \overline{T}_3) + \kappa_s(T_2' - T_3') \tag{12b}$$

where κ_n and κ_s are parameters related to thermal wind and wind-driven gyre mechanisms and are set to the same value of 0.307 Sv °C^{-1}. In this specific setup, $\overline{q_n}$ and $\overline{q_s}$ are calculated as 5.9 Sv and 5.1 Sv, respectively, which correspond to northward and southward heat transports of about 0.46 PW and 0.34 PW, respectively. Furthermore, the equilibrium northward (southward) salinity transport is estimated to be 17.7 (15.8) Sv psu. These equilibria are close to the values simulated by many complex models (Vallis and Farneti 2009; Treguier et al. 2014).

a. Effects of wind-driven circulation

Figure 5 shows dependences of Re(ω) and Im(ω) on λ, using the parameters listed in Table 1. Re(ω) in the 6TS_THC model is smaller than that in the 6S model (Figs. 5a, c), suggesting that thermal processes play a dampening role in the AMOC MCO. Detailed discussion about the impact of the thermal processes on the thermohaline circulation can be found in our publication of YYL23. With the wind-driven circulation, Re(ω) becomes even smaller and the multicentennial mode becomes more damped under the same λ (Figs. 5a, c). When λ = 21.3 Sv kg^{-1} m^3, the e-folding times of the multicentennial mode in the 6S, 6TS_THC, and 6TS_THC+WDC models are about 920, –

2800, and –320 years, corresponding a weakly unstable mode, a weakly damped mode, and a strongly damped mode, respectively. These results also suggest that the wind-driven circulation has a strong damping effect in addition to the thermal processes. However, the maximum Im(ω) does not change too much with the added processes (Fig. 5b), which corresponds to the shortest period of about 340±20 years.

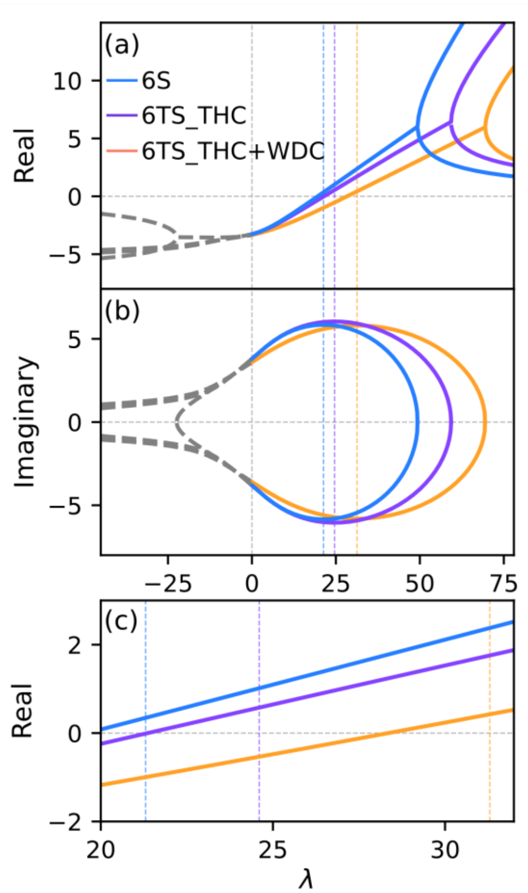

FIG. 5. Dependences of (a) Re(ω) and (b) Im(ω) of multicentennial modes on λ in the 6S, 6TS_THC, and 6TS_THC+WDC models. Solid curves are for $\lambda > 0$; dashed curves are for $\lambda \leq 0$ and have no physical meaning. The vertical dashed blue, purple, and orange lines are for $\lambda = 21.3$, $\lambda = 24.6$, and $\lambda = 31.3$ Sv kg^{-1} m^{3}, respectively. The units of the ordinate are 10^{-10} s^{-1}. Parameters used here are listed in Table 1. (c) Same as (a), but the abscissa axis is zoomed-in. Colored lines are noted in panel (a).

The eigenmodes in the 6TS model under $\lambda = 21.3$ Sv kg^{-1} m^{3} are too damped to become a self-sustained oscillation. Given the higher sensitivity of the overturning circulation to the density change, for example, $\lambda = 24.6$ Sv kg^{-1} m^{3}, the multicentennial mode in the 6TS_THC model has a period of about 330 years and an e-folding time of 550 years. Set $\lambda = 31.3$ Sv kg^{-1} m^{3} in the 6TS_THC+WDC model, the multicentennial mode has a period of 340 years and an e-folding time of 740 years (Table

2). Such an alternative of λ value corresponds to the maximum Im(ω) (the shortest period) and produces the weakly unstable eigenmode (Fig. 5), which can be easily converted to a self-sustained oscillation when enhanced vertical mixing is added in the subpolar North Atlantic.

TABLE 2. Eigenvalues (ω; 10^{-10} s^{-1}) in 6TS model. Particular parameters are k_n = k_s = 0, λ = 24.6 Sv kg^{-1} m^3, $\bar{q}$ = 24 Sv in the 6TS_THC model, k_n = k_s = 0.307 Sv ℃$^{-1}$, λ = 31.3 Sv kg^{-1} m^3, $\bar{q}$ = 24 Sv in the 6TS_THC+WDC model, and k_n = k_s = 0.307 Sv ℃$^{-1}$, λ = 0, $\bar{q}$ = 0 in the 6TS_WDC model. For comparison, the modes of the 6S model are also listed here.

	6S	6TS			Physical meaning
	THC	THC	THC+WDC	WDC	
In 10^{-10} s^{-1}	0.34±5.85i	0.58±6.05i	0.43±5.81i	/	Oscillatory mode
In Year	933±340i	547±329i	737±343i	/	
In 10^{-10} s^{-1}	–8.34±1.12i	–8.17±0.73i	/	/	Oscillatory mode
In Year	–38±1779i	–39±2729i	/	/	
In 10^{-10} s^{-1}	0	0	0	0	Zero mode
	–19.2	–348, –328, –320, –19.4, –5.6, –3.9, –1.6	–363, –337, –320, –23.3, –14.1, –6.2, –5.7, –4.0, –1.5	–331, –324, –317, –7.2, –3.3	Damped mode

Adding enhanced vertical mixing in the subpolar North Atlantic boxes in the 6TS model [Eq. (9)], the equations become,

$$V_1\dot{T}_1' = \cdots - k_m(T_1' - T_4') \tag{13a}$$

$$V_4\dot{T}_4' = \cdots + k_m(T_1' - T_4') \tag{13b}$$

$$V_1\dot{S}_1' = \cdots - k_m(S_1' - S_4') \tag{13c}$$

$$V_4\dot{S}_4' = \cdots + k_m(S_1' - S_4') \tag{13d}$$

Here, λ is set to 24.6 and 31.3 Sv kg^{-1} m^3 for the 6TS_THC and 6TS_THC+WDC models, respectively. The results are obtained from numerical integrations of these models. The self-sustained MCO is manifested in all variables, such as S_1', T_1', and q' (Fig. 6). The presence of the wind-driven circulation weakens the amplitude of the oscillation remarkably (Figs. 6a-c), with the amplitude of q' weakened by about 30% (from 0.35 to 0.23 Sv) (Fig. 6c), while it only lengthens the oscillation period slightly, with the period changing from ~330 to 340 years (Fig. 6f).

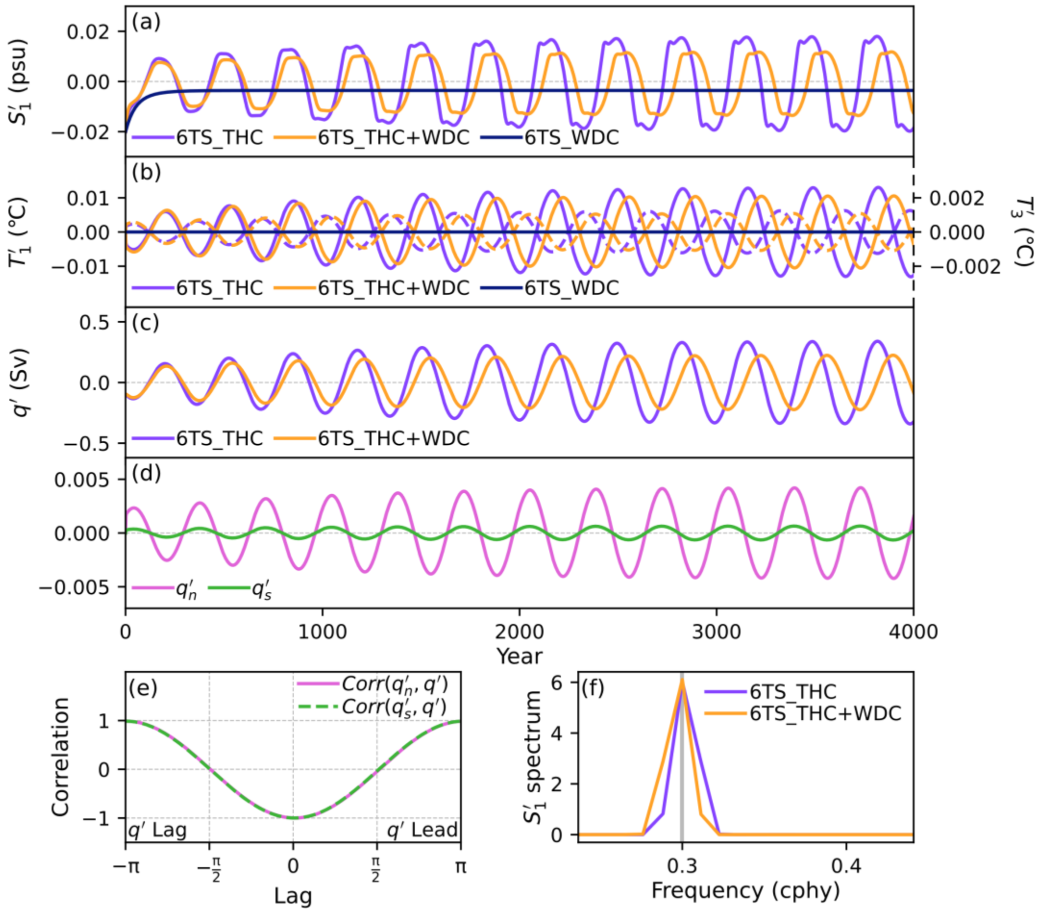

FIG. 6. Time series of (a) S_1' (units: psu) and (b) T_1' and T_3' (units: ℃) in the 6TS_THC, 6TS_THC+WDC, and 6TS_WDC models. In (b), solid (dashed) curves are for T_1' (T_3'). (c) Time series of q' (units: Sv) in these models. (d) Time series of northward q_n' and southward q_s'. (e) Lead-lag correlation coefficients of q' with q_n' and q_s'. For negative lags, q_n' and q_s' lead. (f) Power spectra of S_1' in 6TS_THC and 6TS_THC+WDC; the abscissa is cycle per a hundred year (cphy). The values of λ in the three cases are listed in Table 2. Other parameters use the values in Table 1.

The mechanism of the wind-driven circulation affecting the multicentennial mode in the 6TS_THC+WDC model can be explained as follows. There is a compensation effect between the wind-driven and thermohaline circulations. As shown in Fig. 6e, q_n' and q_s' are inversely related to q'; q_n' is much larger and more important than q_s' (Fig. 6d). There are two negative feedbacks between q' and q_n' in the North Atlantic. Starting with a positive perturbation of q', the perturbation advection $q'(\overline{T}_2 - \overline{T}_1)$ transports more warm water northward, reducing the meridional temperature difference and leading to an increase of T_1' and to decreases of $T_2' - T_1'$ and q_n'. Hence, with increasing q', the weakened q_n' transports less tropical saline water northward by decreasing the perturbation advection of mean salinity [$q_n'(\overline{S}_2 - \overline{S}_1)$], resulting in declines of S_1' and q' (Fig. 7c). Another negative feedback is related to the mean advection $[\overline{q_n}(S_2' - S_1')]$ via the wind-driven circulation, playing a similar role with the mean advection $[\bar{q}(S_2' - S_1')]$ via the thermohaline circulation. Increasing q' leads to increasing S_1' through perturbation advection $[q'(\bar{S}_2 - \bar{S}_1)]$ via the thermohaline circulation, which results in a decline of the mean advection $[\overline{q_n}(S_2' - S_1')]$ by the wind-driven circulation and, in turn, restrains S_1' and q' (Fig. 7c).

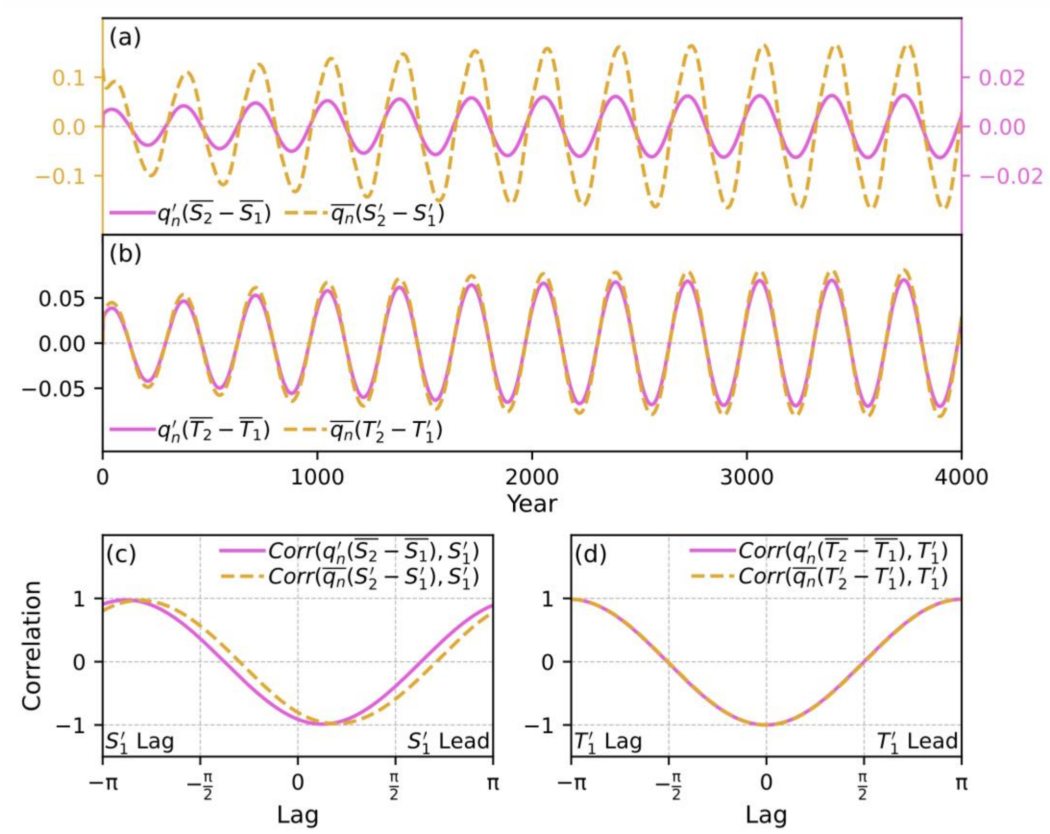

FIG. 7. (a) Time series of salinity terms by the wind-driven circulation (units: Sv psu) in Eq. (9g), which are $q_n'(\bar{S}_2 - \bar{S}_1)$ and $\overline{q_n}(S_2' - S_1')$ in the 6TS_THC+WDC model. (b) Time series of temperature terms (units: Sv ℃) by the wind-driven circulation in Eq. (9a), which are $q_n'(\bar{T}_2 - \bar{T}_1)$ and $\overline{q_n}(T_2' - T_1')$ in the 6TS_THC+WDC model. (c) Lead-lag correlation coefficients of S_1' with $q_n'(\bar{S}_2 - \bar{S}_1)$ and $\overline{q_n}(S_2' - S_1')$. (d) Lead-lag correlation coefficients of T_1' with $q_n'(\bar{T}_2 - \bar{T}_1)$ and $\overline{q_n}(T_2' - T_1')$. For negative lags, salinity and temperature terms lead. λ is set to 31.3 Sv kg^{-1} m^3, and other parameters use the values in Table 1.

Contrary to the salinity processes, the wind-driven thermal processes affect the multicentennial mode through two positive feedbacks (Fig. 7d). The first one is the positive feedback caused by mean wind-driven advection $[\overline{q_n}(T_2' - T_1')]$. With the positive perturbation of q', the growth of T_1' reduces the mean wind-driven advection $[\overline{q_n}(T_2' - T_1')]$, which in turn reduces T_1' and helps promote q'. The second one is the positive feedback of perturbation wind-driven advection $[q_n'(\bar{T}_2 - \bar{T}_1)]$. With the positive perturbation of q' thereby negative perturbation of q_n', the perturbation advection

$[q_n'(\overline{T}_2 - \overline{T}_1)]$ transports less equatorial warm water northward, restraining the rise of T_1' (Fig. 7d) and promoting q'.

Southward wind-driven advection plays a less prominent role in affecting the MCO due to the smaller variability of S_3' and T_3' (Figs. 3a, 6b). The compensation effect between the wind-driven and thermohaline circulations is also valid in the Southern Hemisphere (Fig. 6e). As an increased q' transports more cold water from the subpolar South Atlantic to the tropics through perturbation thermohaline advection, T_2' decreases, resulting in declines of $T_2' - T_3'$ and q_s'. Then, the weakened q_s' transports less warm and saline water from the tropics into the subpolar South Atlantic by decreasing the perturbation advection, $q_s'(\overline{S}_2 - \overline{S}_3)$ and $q_s'(\overline{T}_2 - \overline{T}_3)$. As a result, both S_3' and T_3' decrease (Figs. 8c, d), which tend to help and restrain the growth of q', respectively. The other feedback is related to the mean wind-driven advection, $\overline{q_s}(S_2' - S_3')$ and $\overline{q_s}(T_2' - T_3')$, playing opposite roles against the mean advection feedback of the thermohaline circulation and decreasing both S_3' and T_3'. In short, the southward wind-driven transport affects the MCO through the positive feedback induced by salinity processes and negative feedback induced by thermal processes; however, these feedbacks (Figs. 8a, b) are much weaker than those in the North Atlantic (Figs. 7a, b).

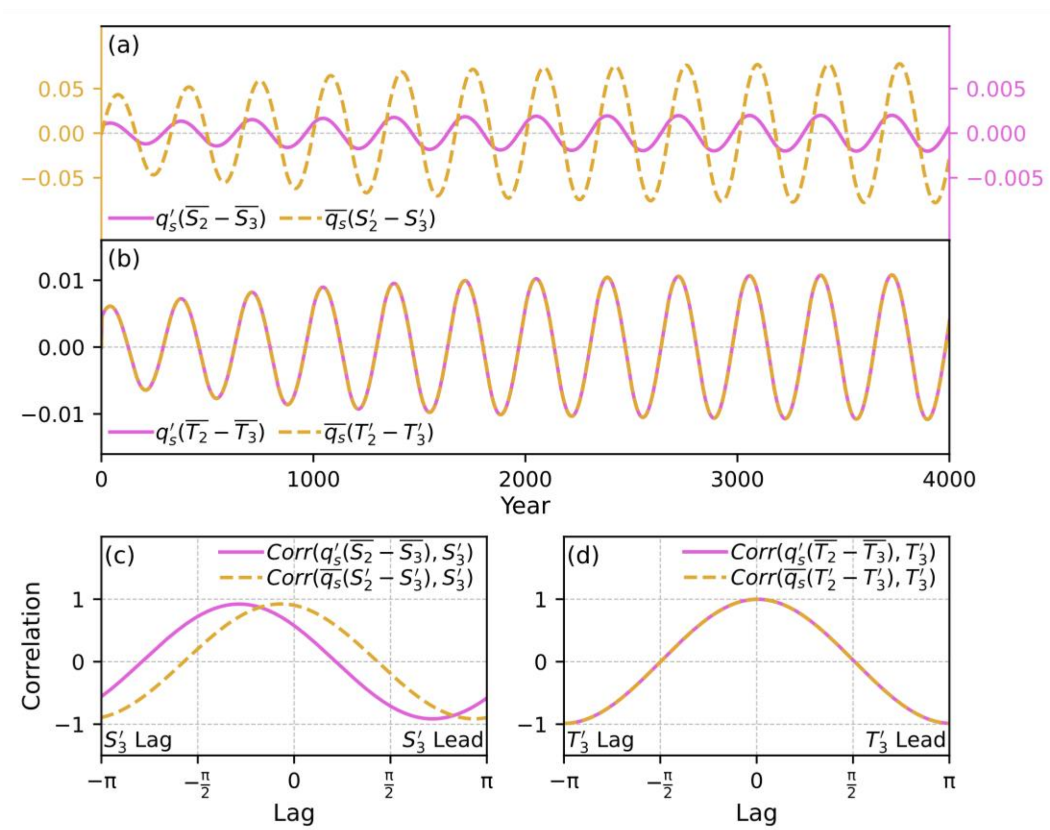

FIG. 8. Same as Fig. 7, but for the wind-driven circulation in the subpolar Southern Hemisphere.

b. Stability analysis in the presence of wind-driven circulation only

To demonstrate the essential role of the thermohaline circulation in the MCO, we shut it down (i.e., $\bar{q}$ = 0 and λ = 0), so there is only the wind-driven circulation in the box model. Temperature and salinity anomalies show no oscillation once the thermohaline circulation is shutdown (navy blue curves in Figs. 6a, b). Now the system has only heat and salinity transports in the upper ocean by the wind-driven circulation, in which the variability is controlled only by the temperature variability in the upper ocean. Eqs. (9a-c) can be rewritten as follows,

$$V_1\dot{T}_1' = -V_1\gamma T_1' + \overline{q_n}(T_2' - T_1') + q_n'(\bar{T}_2 - \bar{T}_1) \tag{14a}$$

$$V_2\dot{T}_2' = -V_2\gamma T_2' - \overline{q_n}(T_2' - T_1') - q_n'(\bar{T}_2 - \bar{T}_1) - \bar{q}_s(T_2' - T_3') - q_s'(\bar{T}_2 - \bar{T}_3) \tag{14b}$$

$$V_3\dot{T}_3' = -V_3\gamma T_3{}' + \bar{q}_s(T_2' - T_3') + q_s'(\bar{T}_2 - \bar{T}_3) \tag{14c}$$

Subtracting Eq. (14a) and Eq. (14c) from Eq. (14b), respectively, we have,

$$\dot{T}_n' = (\sigma_1(\overline{q_n} + \kappa_n\overline{T_n}) - \gamma)T_n' + \sigma_2(\bar{q}_s + \kappa_s\bar{T}_s)T_s' \tag{15a}$$

$$\dot{T}_s' = \sigma_2(\overline{q_n} + \kappa_n\overline{T_n})T_n' + (\sigma_3(\bar{q}_s + \kappa_s\bar{T}_s) - \gamma)T_s' \tag{15b}$$

where $\overline{T_n} = \bar{T}_2 - \bar{T}_1$, $\bar{T}_s = \bar{T}_2 - \bar{T}_3$, $\sigma_1 = \frac{1}{V_1} - \frac{1}{V_2}$, $\sigma_2 = -\frac{1}{V_2}$, and $\sigma_3 = \frac{1}{V_3} - \frac{1}{V_2}$.

With $\overline{q_n} = \kappa_n\overline{T_n}$ and $\bar{q}_s = \kappa_s\bar{T}_s$, we can further define the following quantities:

$$C_1 = \sigma_1(\overline{q_n} + \kappa_n\overline{T_n}) - \gamma = 2\sigma_1\overline{q_n} - \gamma$$
$$C_2 = \sigma_2(\bar{q}_s + \kappa_s\bar{T}_s) = 2\sigma_2\bar{q}_s$$
$$C_3 = \sigma_2(\overline{q_n} + \kappa_n\overline{T_n}) = 2\sigma_2\overline{q_n}$$
$$C_4 = \sigma_3(\bar{q}_s + \kappa_s\bar{T}_s) - \gamma = 2\sigma_3\bar{q}_s - \gamma$$

Assuming the solution has the form of $T_n' = Ae^{\omega t}$, Eq. (15) has eigenvalues,

$$\omega = \frac{1}{2}\left[(C_1 + C_4) \pm \sqrt{(C_1 + C_4)^2 - 4(C_1C_4 - C_2C_3)}\right] \tag{16}$$

The eigenvalues lie on the value Δ that is defined by,

$$\Delta = (C_1 + C_4)^2 - 4(C_1C_4 - C_2C_3) = [4(\sigma_1\overline{q_n} - \sigma_3\bar{q}_s)^2 + 16\sigma_2{}^2\overline{q_n}\bar{q}_s] > 0 \tag{17}$$

Here, Δ is always positive; and there will be no oscillatory solutions in this system, as long as the wind-driven circulation transports heat and salinity poleward (i.e., $\overline{q_n}$ > 0 and $\bar{q}_s$ > 0). In fact, Eq. (14) clearly shows that the tendencies of T_1', T_2', and T_3' are always damped by T_1', T_2', and T_3' themselves. As the temperature anomaly increases, its tendency will be in turn killed. The theoretical solution in the presence of only wind-driven circulation agrees well with the numerical results in section 4a.

From another perspective, the inclusion of the northward (southward) wind-driven circulation offers two negative (positive) salinity feedbacks and two positive (negative) temperature feedbacks, which are unable to produce oscillations. In other words, the MCO can only be possible in the presence of the thermohaline circulation, which can produce both negative and positive feedbacks for the thermal and saline processes simultaneously, which are necessary to induce low-frequency oscillation.

5. Linear oscillations excited by stochastic forcing

In this section, we further investigate the AMOC MCO under stochastic forcing, following the approach in LY22. With the inclusion of the stochastic freshwater and heat inputs in the subpolar North Atlantic, Eq. (3a) is rewritten as follows,

$$V_1\dot{S}_1' = \cdots + V_1 N \tag{18a}$$

$$V_1\dot{T}_1' = \cdots + V_1 N \tag{18b}$$

where N represents the external stochastic forcing, which is a red noise generated from the model of Auto-Regressive-1 and has an autocorrelated e-folding decay time of 10 years. λ is set to 21.0 and 23.0 Sv kg^{-1} m^3 for the 6TS_THC and 6TS_THC+WDC models, respectively, indicating that the internal oscillations are damped oscillations due to the negative real part of the eigenmodes (Fig. 5a). Other parameters are the same as those in Table 1.

Stochastic forcing can turn such damped oscillatory mode into a sustained oscillation even without enhanced vertical mixing (Figs. 9a-c). The ratio of the S_1' spectrum (Fig. 9f) to the spectrum of the noise (Fig. 9d), i.e., signal-to-noise ratio (SNR), is shown in Fig. 9g, in which the SNR reaches a maximum at the period of about 320 years. This principal period is identical to the period obtained from the linear stability analysis in section 2, suggesting that the multicentennial mode is an intrinsic mode of the Atlantic Ocean. Furthermore, it is clear that the wind-driven circulation plays a damping role in the oscillation (Figs. 9a-c) and lengthens its period slightly (Fig. 9g). After adding the wind-driven circulation, the SNR has a lower power with the peak value corresponding to 340 years (orange curve in Fig. 9g). Once the thermohaline circulation is shut down, the SNR has no peak (blue curve in Fig. 9g), suggesting no preferred period in the system.

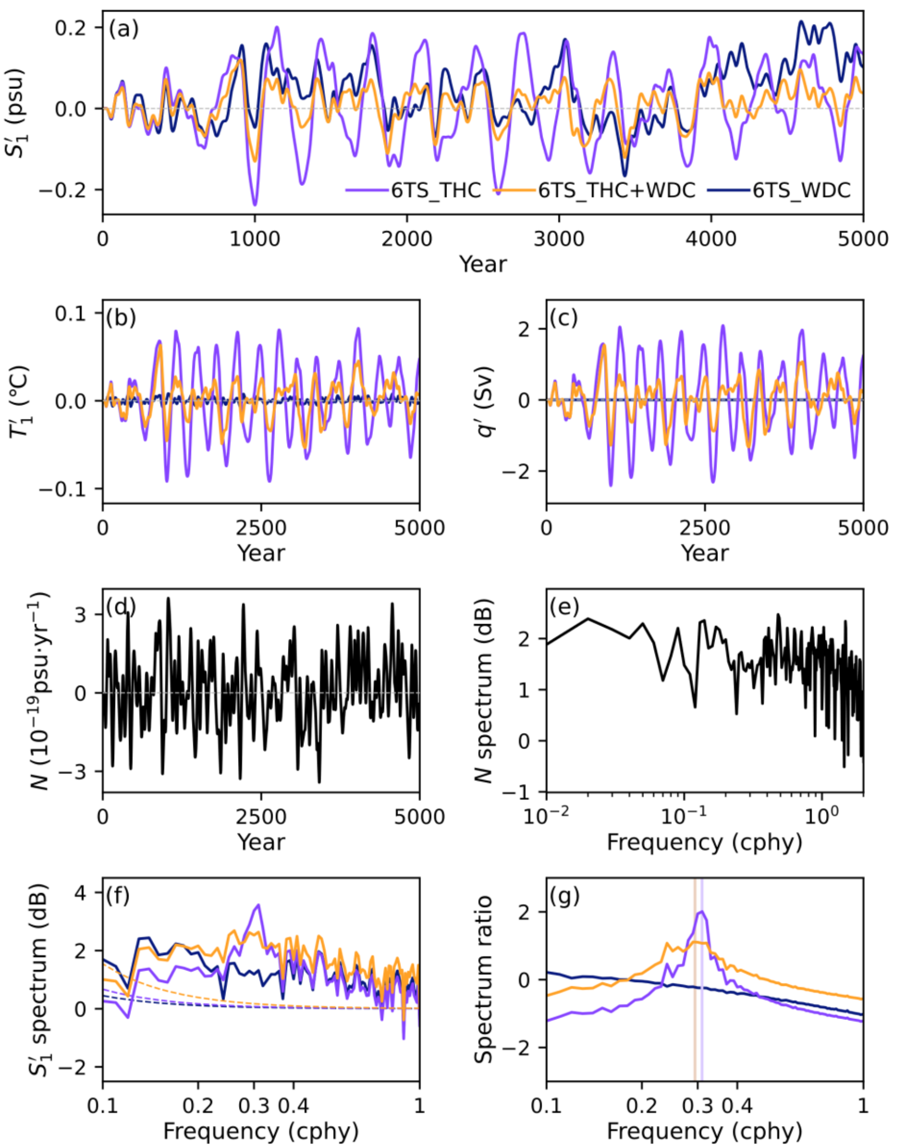

FIG. 9. Time series of (a) S_1', (b) T_1', and (c) q' in the 6TS_THC model, the 6TS_THC+WDC model, and the 6TS_WDC model, forced by stochastic freshwater and heat flux. λ is set to 21.0 and 230 Sv kg^{-1} m^3 for the 6TS_THC and 6TS_THC+WDC modes, respectively; and damped oscillatory modes are obtained in the presence of the thermohaline circulation. Other parameters take the values in Table 1. (d) Time series of stochastic freshwater and heat flux (units: 10^{-19} psu yr^{-1} and 10^{-19} °C yr^{-1}), which is red noise; and (e) their power spectra (units: dB). (f) The power spectra of S_1' for three cases with the confidence level 95%. (g) The ratios of S_1' spectrum to the noise spectrum (units: dB), with peaks around 0. 31 and 0. 29 cycles per a hundred year (cphy) (320 and 340 years) for the 6TS_THC and 6TS_THC+WDC modes, respectively. Colored curves are noted in panel (a).

6. Summary and discussion

In this study, we investigate the AMOC MCO in a two-hemisphere box model, which is an advancement from our proposed one-hemispheric theoretical model (LY22; YYL23). In the two-hemisphere model, the AMOC anomaly is parameterized to be linearly proportional to the density difference between the northern and southern subpolar boxes. This parameterization represents the competition between the NADW and AABW, which is a crucial element for AMOC variability. An MCO mode with a period of about 340 years is identified in the two-hemisphere box model under the parameters in Table 1. These results align with the findings of LY22, indicating comparable periods in the one-hemisphere and two-hemisphere models, because both the total ocean basin volume and mean AMOC strength in this study are approximately twice of those in LY22. Similar to LY22 and YYL23, the sustained MCO can be easily excited by external stochastic forcing, suggesting that this MCO is an intrinsic mode of the global ocean.

The wind-driven circulation plays a dampening effect on the AMOC MCO. The primary effect of the wind-driven circulation is to weaken the amplitude of the AMOC MCO, as its effect on the MCO period can be neglected. The stabilized effect of the wind-driven circulation occurs because of the negative feedback between the thermohaline and wind-driven circulations through the salinity processes in the North Atlantic. The compensation between the strengths of thermohaline and wind-driven circulations occurs because a stronger thermohaline circulation causes a stronger meridional heat transport, which, in turn, reduces the meridional temperature gradient, weakening the wind-driven circulation. This further leads to less poleward salinity transport and slows down the growth of salinity anomaly in the subpolar North Atlantic, resulting in the weakening of the AMOC MCO. Note that the wind-driven circulation alone cannot cause oscillatory behavior in such a two-hemisphere box model. Once the thermohaline circulation is shut down, the MCO ceases to exist, suggesting that the thermohaline circulation is a necessary condition in generating the MCO. The 6TS model including the wind-driven circulation is more realistic, since the oceanic thermal processes and the Southern Ocean are included simultaneously.

To better understand eigenmodes in the two-hemisphere box model, a further simplified version of the 6S model, referred to as the 3-box model (the 3S model; Appendix B, Fig. B1), is constructed. Despite its simplicity, the 3S model gives a nearly identical oscillatory eigenmode to that of the 6S model (Fig. B1), and to that reported in Scott et al. (1999) as well, under similar parameters. This suggests that the simplification of the box structure and basin geometry in the 3S model does not change the fundamentals of the multicentennial eigenmode found in the 6S model; thus, the theoretical solution of the 3S model can offer a deeper understanding of the mechanism driving the

MCO mode. For example, as detailed in Appendix B, the theoretical solution to the MCO period in the 3S model can be written as,

$$T \sim \frac{2\pi}{\bar{q}}\left(\frac{V_1 V_2}{\frac{V_2}{V_1}M^2-\left(\frac{V_2}{V_1}-\frac{V_2}{V_3}+1\right)M+1}\right)^{\frac{1}{2}}, \text{ where } M=\frac{V_3}{V_2}\left(\frac{V_2F_{w1}-V_1F_{w2}}{V_3F_{w1}-V_1F_{w3}}\right), \quad (19)$$

which indicates that the mean AMOC strength, the basin volume and geometry, and surface freshwater fluxes in different ocean basins can affect the oscillation period significantly.

In both the 6S and 3S models, we observe a linear relationship between total basin volume and oscillatory period, and an inversely proportional relationship between the mean AMOC strength and the oscillatory period (Fig. 10). In larger ocean basins, such as the Pacific Ocean, the period of the MCO could be much longer (Fig. 10a), if the thermohaline circulation exists in the Pacific instead of in the Atlantic. This could have occurred in the Earth's history (Okazaki et al. 2010; Burls et al. 2017). Paleoclimatic evidence has suggested that the NADW formation began around 15 million years ago, before which the deep-water formation may have occurred in the North Pacific (Okazaki et al. 2010). It is then straightforward that the weaker the AMOC strength is, the longer period the MCO has (Fig. 10b). It is interesting to notice that there could have millennial oscillation in the global ocean with period of about 1500 years, if the mean AMOC is half of the value of the present climate (Fig. 10b). This might provide a clue to understand the Dansgaard-Oeschger cycle (the D-O cycle; Dansgaard et al. 1984) during the LGM or the Bond cycles (Bond et al. 1997) during the Holocene.

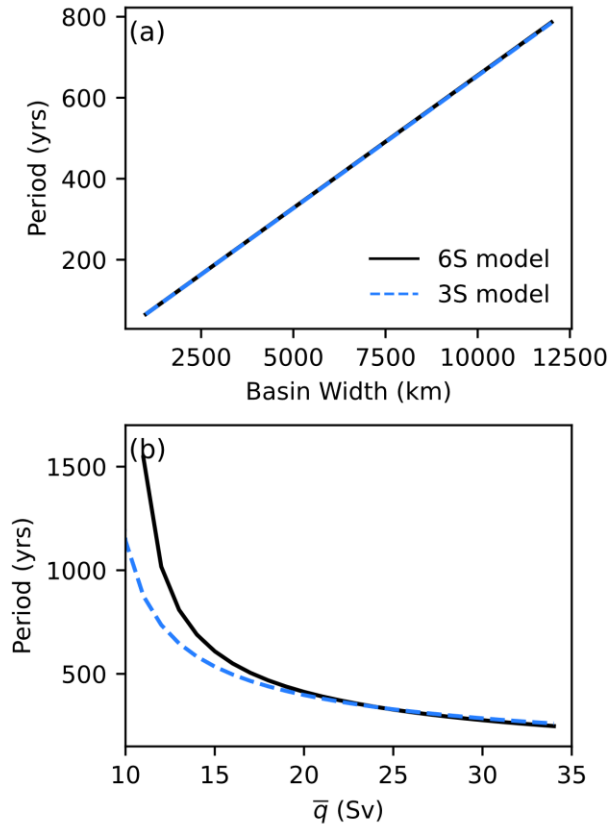

FIG. 10. Dependences of the minimum period of the multicentennial oscillatory mode on (a) mean basin width and (b) $\overline{q}$ in the 6S and 3S models, respectively. The black curve is the results from the numerical solutions of the 6S model. The dashed blue curve is the results from the theoretical solution of the 3S model.

In addition to the total basin volume, the basin geometry plays a significant role in determining the period of the AMOC MCO, as shown in Fig. 4 and Eq. (19). This basin geometry encompasses various factors, such as the depth of the upper and lower oceans, the division between the tropics and extratropics, the definition of the deep-water formation region, and so on. The basin geometry offers numerous possibilities; and it is not immediately evident that the MCO would have a specific period. However, under a “reasonably realistic” basin geometry, it is highly likely that the ocean would exhibit an oscillation with a centennial to millennial timescale, known as the MCO.

The MCO period is also closely related to climatological surface freshwater fluxes in different basins [Eq. (19)]. The sensitivity of the MCO to surface freshwater flux is complex, and is not studied in this paper, because changes in the mean surface freshwater flux may lead to regime shift and multi-equilibrium states of the climate system. Therefore, surface freshwater flux is simply prescribed in this paper. The mean surface freshwater flux determines equilibrium salinity, which, in turn, determines the linear closure parameter λ (Appendix B, Eq. (B14)). Besides, Eq. (B8) reveals the significant interaction between surface freshwater flux and closure parameter λ. However, we also found that under certain conditions, the surface freshwater flux did not have a significant impact on the MCO period. For example, when the equilibrium salinity of the subpolar South Atlantic is equal to that of the other regions (i.e., $\overline{S_2} = \overline{S_3}$ or $\overline{S_1} = \overline{S_3}$), the MCO period only depends on the basin geometry and the strength of the AMOC (Appendix B, Eqs. (B16) and (B17)). The derivation in Appendix B indicates a clear physical connection between the surface freshwater flux and MCO; further studies will be carried out in the future.

Although the MCO can be an intrinsic mode of the thermohaline circulation, its sustainability in the real world is a serious concern. The AMOC MCO is strongly influenced by changing climate background, such as variations in sea-surface freshwater flux, the deep-water formation region, the AMOC strength, etc. In unfavorable environmental conditions, the detection of the AMOC MCO in the real world might be challenging, which may explain the weak signals of the MCO retrieved from proxy data (Stocker and Mysak 1992).

Besides the possibility that the MCO might become the millennial timescale in the climate with a weak AMOC (Fig. 10b), there is a millennial mode in the two-hemisphere box model (Figs. 2c, d). Even though the physical meaning of this millennial mode is unclear, it might also provide a clue for understanding the D-O cycle and Bond cycles. Inspired by Sakai and Peltier (1995, 1996, 1997), which reported that increased surface freshwater fluxes could lengthen the period of the MCO to the millennial timescale, we plan to conduct a study aiming to excite the millennial oscillation, with a focus on the influence of surface freshwater flux from the Arctic sea ice and Antarctic ice sheet. We will develop an air-sea coupled box model , in which a varying surface freshwater flux can be introduced. We hope to not only deliberate the sensitivity of the MCO to surface freshwater fluxes, but also identify a less damped millennial mode. Such results may shed light on mechanisms of long-term climate evolution since the LGM.

Acknowledgements.

This research is jointly supported by the NSF of China (Nos. 42230403, 42288101, 41725021, and 91737204) and by the foundation at the Shanghai Frontiers Science Centre of Atmosphere-Ocean Interaction of Fudan University.

Data Availability Statement.

This is a theory-based article; thus, no datasets are generated.

APPENDIX A

Linear relation between AMOC and meridional density difference in the Atlantic

Studies have demonstrated a linear relation between the AMOC index and the density difference between the North Atlantic and South Atlantic, despite that the regions selected may be different (Hughes and Weaver 1994; Rahmstorf 1996; Thorpe et al. 2001; Griesel and Maqueda 2006; Wood et al. 2019). Here, we validate the parameterization of the AMOC index in the two-hemispheric box model utilizing results from two coupled climate models, namely the Community Earth System Model (CESM, version 1.0) developed by the National Centre for Atmospheric Research (NCAR) and EC-Earth3-Veg-LR. The AMOC index is defined as the maximum meridional streamfunction in the region of 20°-70°N between 200 and 3000 m in the Atlantic. The meridional density difference is defined by taking the difference in density anomalies integrated over a depth of 4000 m between a North Atlantic box and a South Atlantic box. The North Atlantic box covers the region of 40°-50°W, 43°-60°N; the South Atlantic 25°-50°W, 45°-55°S; and the subtropic box, 20°-65°W, 20°-35°N (Fig. A1a). These definitions are applied in the same way for both coupled models.

A long simulation using the CESM1.0 was reported in Yang et al. (2015). The ocean component of CESM1.0 is the Parallel Ocean Program version 2 (POP2; Smith et al. 2010) and employs the gx1v6 curvilinear grid, comprising 384 × 320 grid points horizontally and 60 layers vertically. The zonal spacing within the ocean grid is uniformly set at 1.1258, while the meridional spacing varies non-uniformly: near the equator, the resolution is 0.278°, gradually increasing to a maximum of 0.65° at 60°N/S, and then tapering off toward the poles. Detailed configurations can be found in Yang et al. (2015). The simulation starts from a state of rest with the standard configuration for the preindustrial condition, and is integrated for 2500 years. For analysis, we use the data from the final 1900 years of the simulation.

In the CESM1.0 simulation, the mean salinity is 33.9 psu for the surface North Atlantic box and 33.7 psu for the surface South Atlantic box (Fig. A1a). The mean temperatures are 4.9 ℃ and 5.4 ℃ for the northern and southern boxes, respectively. The subtropic box, comprising regions of maximum surface salinity in the Atlantic, has mean salinity of 36.8 psu and mean temperature of 23.5 ℃. The mean AMOC is about 24 Sv.

Figure A1b shows the linear regression pattern of the AMOC index on the density anomalies over 4000-m depth. There is a strong positive (negative) correlation between the AMOC anomaly and the salinity anomaly in the subpolar North (South) Atlantic box. Figures A1c and d show the scattering plots of the AMOC anomaly versus the density difference between the North Atlantic and South Atlantic, and their time series. There is a strong positive, linear correlation between them, with a correlation coefficient of 0.89.

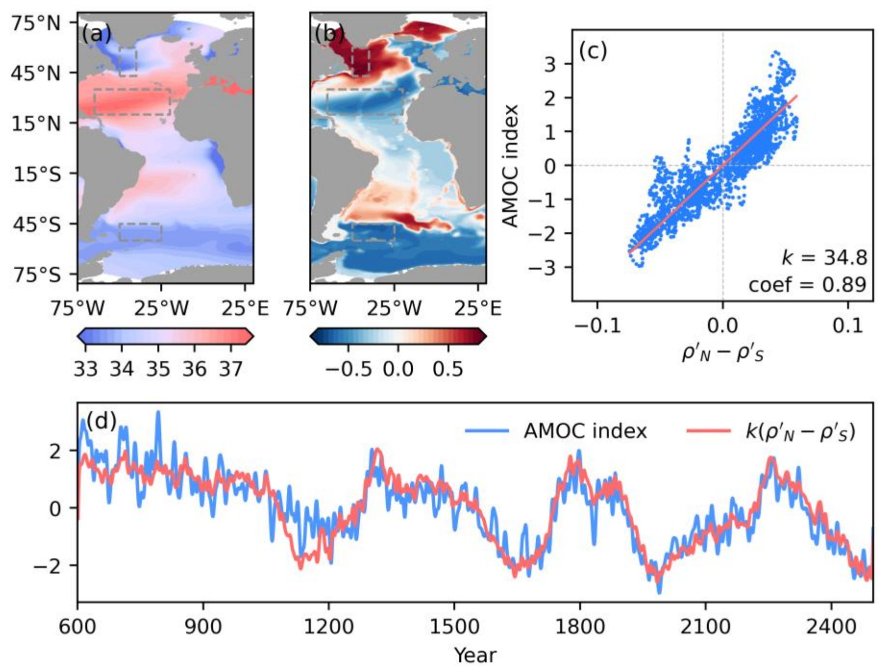

FIG. A1. (a) Climatology of sea-surface salinity (units: psu) in CESM 1.0. Dashed boxes outline the subpolar North, tropical, and subpolar South Atlantic boxes, respectively. (b) Regression of AMOC anomaly (units: Sv) on density anomaly integrated above 4000-m depth (units: kg m^{-3}). (c) Scatter plot of AMOC anomaly (ordinate) versus the difference of density anomaly (abscissa) averaged between the two regions in subpolar North and South Atlantic oceans, respectively. The red line represents the reduced major axis regression with a coefficient of 0.89 and a slope of 34.8 Sv kg^{-1} m^3. (d) Time series of AMOC anomaly (blue curve) and its estimation (red curve) from the reduced major axis regression. In (c) and (d), the anomalies of AMOC index and density are lowpass-filtered with a cutoff period of 10 years.

A 500-year simulation of the EC-Earth3-Veg-LR model output was obtained from the World Climate Research Program (WCRP) Coupled Model Intercomparison Project, Phase 6 (CMIP6) data, provided by the EC-Earth-Consortium team for the “pre-industrial control” (piControl) experiment. The ocean component of the model utilized version 3.6 of the Nucleus for European Modelling of the Ocean (NEMO3.6) in the ORCA1 configuration. This configuration uses a tripolar grid of poles, and comprises 362 x 292 horizontal grids and 75 vertical levels. The spatial resolution was predominantly set at 1 degree, with a refined resolution of 1/3 degrees in the tropics. Detailed information regarding the model and its configuration can be found in Döscher et al. (2022).

In the EC-Earth3-Veg-LR simulations, the mean salinity is 32.5 psu for the surface North Atlantic box and 33.7 psu for the surface South Atlantic box (Fig. A2a). The mean temperatures are 3.5 ℃ and 6.9 ℃ for the northern and southern boxes, respectively. The subtropic box has mean salinity of 36.7 psu and mean temperature of 22.7 ℃. The mean AMOC is about 18 Sv.

Figure A2b shows the linear regression pattern of the AMOC index on the density anomalies over 4000-m depth. Figures A2c and d show the scattering plots of the AMOC anomaly versus the density difference between the North Atlantic and South Atlantic, and their time series. There is also a strong positive, linear correlation between them, with a correlation coefficient of 0.81.

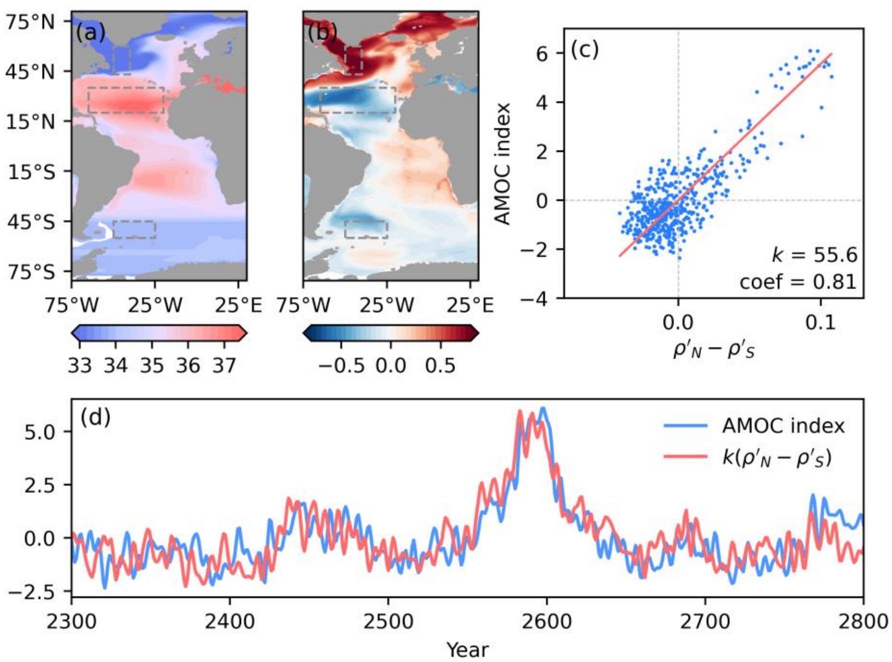

FIG. A2. Same as Fig. A1, but for EC-Earth3-Veg-LR simulation results. The regression coefficient in (b) is 0.81, and the slope is 55.6 Sv kg^{-1} m^3. The cutoff period for filtering in (d) is five years.

APPENDIX B

Theoretical solution to the multicentennial oscillatory mode

Similar to LY22, if we consider extreme mixing in the subpolar North Atlantic, the 6S model can be reduced to a 5-box model, namely the 5S model (Fig. B1a). Eq. (3) can be simplified as follows,

$$V_1\dot{S}_1' = \bar{q}(S_2' - S_1') + q'(\bar{S}_2 - \bar{S}_1) \tag{B1a}$$

$$V_2\dot{S}_2' = \bar{q}(S_3' - S_2') + q'(\bar{S}_3 - \bar{S}_2) \tag{B1b}$$

$$V_3\dot{S}_3' = \bar{q}(S_6' - S_3') + q'(\bar{S}_1 - \bar{S}_3) \tag{B1c}$$

$$V_5\dot{S}_5' = \bar{q}(S_1' - S_5') \tag{B1d}$$

$$V_6\dot{S}_6' = \bar{q}(S_5' - S_6') \tag{B1e}$$

In the 5S model, the eigenmode of the MCO is only slightly different from that in the 6S model (Fig. B2). This is similar to the case in the one-hemisphere box model (LY22).

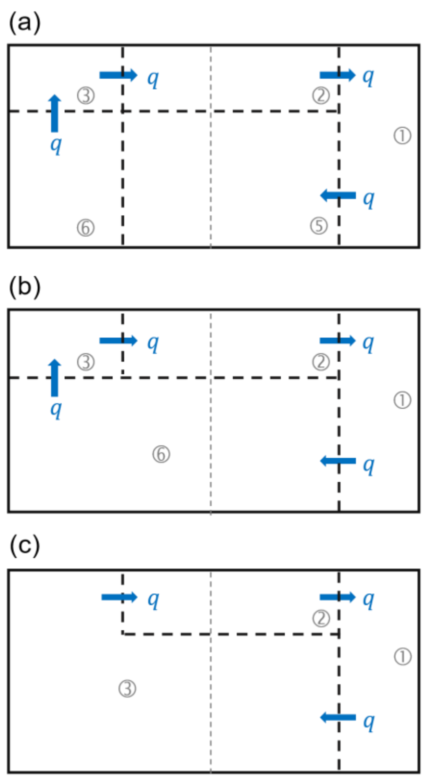

FIG. B1. Schematic diagrams of (a) 5-box model (5S model), and simplified (b) 4-box model (4S model), and (c) 3-box model (3S model). In the 5S model, the two subpolar North Atlantic boxes are merged, representing the enhanced mixing there. In the 4S model, the lower oceans in the equatorial and subpolar South Atlantic are combined into one box; in the 3S model, the whole subpolar South Atlantic is further merged with the equatorial lower oceans.

To solve the eigenvalues in the two-hemisphere box model, the 5S model can be further simplified to a 4-box model (namely the 4S model) by merging the deep ocean box at the equator and South Atlantic, and to a 3-box model (namely the 3S model) by further including the box of the upper South Atlantic, as shown in Fig. B1.

The equations of the 4S model are written as follows,

$$V_1\dot{S}_1' = \bar{q}(S_2' - S_1') + q'(\overline{S_2} - \overline{S_1}) \tag{B2a}$$

$$V_2\dot{S}_2' = \bar{q}(S_3' - S_2') + q'(\overline{S_3} - \overline{S_2}) \tag{B2b}$$

$$V_3\dot{S}_3' = \bar{q}(S_6' - S_3') + q'(\overline{S_1} - \overline{S_3}) \tag{B2c}$$

$$V_6\dot{S}_6' = \bar{q}(S_1' - S_6') \tag{B2d}$$

The equations of the 3S model are written as follows,

$$V_1\dot{S}_1' = \bar{q}(S_2' - S_1') + q'(\overline{S_2} - \overline{S_1}) \tag{B3a}$$

$$V_2\dot{S}_2' = \bar{q}(S_3' - S_2') + q'(\overline{S_3} - \overline{S_2}) \tag{B3b}$$

$$V_3\dot{S}_3' = \bar{q}(S_1' - S_3') + q'(\overline{S_1} - \overline{S_3}) \tag{B3c}$$

Similar to the 6S model, the difference of equilibrium salinity in the 3S model is related to the surface freshwater flux, which is given by,

$$F_{w1} = \bar{q}(\overline{S_1} - \overline{S_2}) \tag{B4a}$$

$$F_{w2} = \bar{q}(\overline{S_2} - \overline{S_3}) \tag{B4b}$$

$$F_{w3} = \bar{q}(\overline{S_3} - \overline{S_1}) \tag{B4c}$$

The eigenvalues of the 3S, 4S, 5S, and 6S models are very similar (Fig. B2). The minimum periods for the 3S, 4S, 5S, and 6S models are about 330, 330, 350, and 340 years, respectively, which indicates that the simplification does not change the fundamentals of the MCO.

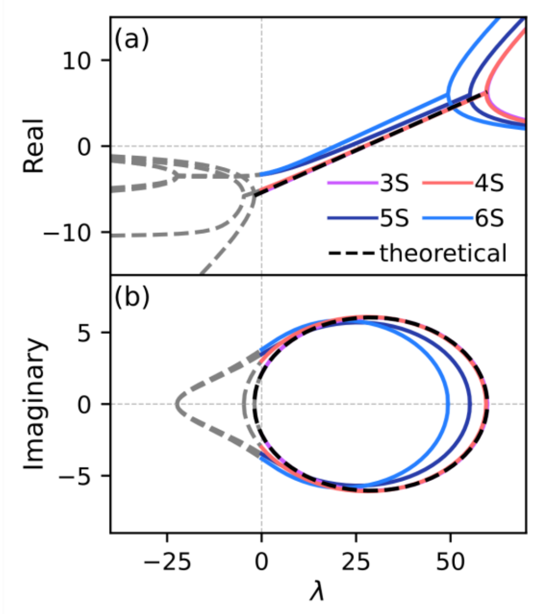

FIG. B2. Dependences of (c) real and (d) imaginary parts of the multicentennial oscillatory modes on λ in the 3S, 4S, 5S, and 6S, respectively. In these models, solid curves are for $\lambda > 0$; dashed gray curves are for $\lambda < 0$. [meaningless?] Dashed black curve represents the theoretical solution to the 3S model. The units of the ordinate are 10^{-10} s^{-1}. The parameters take the values in Table 1.

The 3S model can be solved analytically. By subtracting Eq. (B3a) from Eq. (B3b) and Eq. (B3c), respectively, we obtain,

$$\dot{a}' = (-\sigma_1\bar{q} - \sigma_2\bar{q})a' + (M_{sn}\lambda - M_{ss}\lambda + \sigma_2\bar{q})h' \tag{B5a}$$

$$\dot{h}' = (-\sigma_1\bar{q})a' + (M_{sn}\lambda - M_s\lambda - \sigma_3\bar{q})h' \tag{B5b}$$

where $M_{sn} = \rho_0\beta\frac{\overline{S_2}-\overline{S_1}}{V_1}$, $M_{ss} = \rho_0\beta\frac{\overline{S_3}-\overline{S_2}}{V_2}$, $M_s = \rho_0\beta\frac{\overline{S_1}-\overline{S_3}}{V_3}$, $\sigma_1 = \frac{1}{V_1}$, $\sigma_2 = \frac{1}{V_2}$, and $\sigma_3 = \frac{1}{V_3}$.

Hence, we can define the following quantities:

$$C_1 = -(\sigma_1 + \sigma_2)\bar{q}$$
$$C_2 = (M_{sn} - M_{ss})\lambda + \sigma_2\bar{q}$$
$$C_3 = -\sigma_1\bar{q}$$
$$C_4 = (M_{sn} - M_s)\lambda - \sigma_3\bar{q}$$

Assuming the form of solution as $a' = Ae^{\omega t}$, Eq. (A5) has eigenvalues as follows,

$$\omega = \frac{1}{2}\left[(C_1 + C_4) \pm \sqrt{(C_1 + C_4)^2 - 4(C_1C_4 - C_2C_3)}\right] \tag{B6}$$

If $\Delta = (C_1 + C_4)^2 - 4(C_1C_4 - C_2C_3) < 0$, we have oscillatory solutions, which are,

$$\mathrm{Re}(\omega) = \frac{1}{2}(C_1 + C_4) \tag{B7a}$$

$$\mathrm{Im}(\omega) = \frac{1}{2}(\sqrt{4(C_1C_4 - C_2C_3) - (C_1 + C_4)^2}) \tag{B7b}$$

Eqs. (B6) and (B7) give the theoretical eigenmodes of the 3S model (black curves in Fig. B2a, b), which are consistent with the numerical results.

The period of the oscillation (Δ)lies on the imaginary part of the eigenvalue, which can be rewritten as follows,

$$\begin{aligned}
\Delta &= 4(C_1C_4 - C_2C_3) - (C_1 + C_4)^2 \\
&= -(C_1 - C_4)^2 - 4C_2C_3 \\
&= -(M_{sn}\lambda - M_s\lambda - \sigma_3\bar{q} + \sigma_1\bar{q} + \sigma_2\bar{q})^2 + 4\sigma_1\bar{q}(M_{sn}\lambda - M_{ss}\lambda + \sigma_2\bar{q}) \\
&= -(M_{sn} - M_s)^2\lambda^2 - (\sigma_1 + \sigma_2 - \sigma_3)^2\bar{q}^2 + 4\sigma_1\sigma_2\bar{q}^2 \\
&\quad -2\bar{q}(M_{sn} - M_s)(\sigma_1 + \sigma_2 - \sigma_3)\lambda + 4\sigma_1\bar{q}(M_{sn} - M_{ss})\lambda
\end{aligned} \tag{B8}$$

(B8) suggests that the surface freshwater flux and λ interact to influence the period of the MCO. In other words, the specific value of λ can determine the extent to which the surface freshwater flux impacts the period.

Δ is a quadratic function of λ and has a maximum occurring at,

$$\begin{aligned}
\lambda = \lambda_{max} &= -\frac{-2\bar{q}(M_{sn} - M_s)(\sigma_1 + \sigma_2 - \sigma_3) + 4\sigma_1\bar{q}(M_{sn} - M_{ss})}{-2(M_{sn} - M_s)^2} \\
&= \frac{-\bar{q}(M_{sn} - M_s)(\sigma_1 + \sigma_2 - \sigma_3) + 2\sigma_1\bar{q}(M_{sn} - M_{ss})}{(M_{sn} - M_s)^2}
\end{aligned} \tag{B9}$$

The maximum Δ is determined by,

$$\begin{aligned}
\Delta_{max} &= -(\sigma_1 + \sigma_2 - \sigma_3)^2\bar{q}^2 + 4\sigma_1\sigma_2\bar{q}^2 + \frac{[2\bar{q}(M_{sn} - M_s)(\sigma_1 + \sigma_2 - \sigma_3) - 4\sigma_1\bar{q}(M_{sn} - M_{ss})]^2}{4(M_{sn} - M_s)^2} \\
&= -(\sigma_1 + \sigma_2 - \sigma_3)^2\bar{q}^2 + 4\sigma_1\sigma_2\bar{q}^2 + \left[(\sigma_1 + \sigma_2 - \sigma_3) - 2\sigma_1\frac{M_{sn} - M_{ss}}{M_{sn} - M_s}\right]^2\bar{q}^2 \\
&= -\bar{q}^2[(\sigma_1 + \sigma_2 - \sigma_3)^2 - 4\sigma_1\sigma_2 - (\sigma_1 + \sigma_2 - \sigma_3 - 2\sigma_1M)^2] \\
&= -\bar{q}^2[-4\sigma_1\sigma_2 - 4{\sigma_1}^2M^2 + 4\sigma_1M(\sigma_1 + \sigma_2 - \sigma_3)] \\
&= 4\sigma_1\sigma_2\bar{q}^2\left[1 + \frac{\sigma_1}{\sigma_2}M^2 - \frac{1}{\sigma_2}M(\sigma_1 + \sigma_2 - \sigma_3)\right] \\
&= 4\sigma_1\sigma_2\bar{q}^2\left[1 + \frac{\sigma_1}{\sigma_2}M^2 - \left(\frac{\sigma_1}{\sigma_2} + 1 - \frac{\sigma_3}{\sigma_2}\right)M\right]
\end{aligned} \tag{B10}$$

where $M = \frac{M_{sn}-M_{ss}}{M_{sn}-M_s} = \frac{\frac{1}{V_1}(\overline{S_2}-\overline{S_1})-\frac{1}{V_2}(\overline{S_3}-\overline{S_2})}{\frac{1}{V_1}(\overline{S_2}-\overline{S_1})-\frac{1}{V_3}(\overline{S_1}-\overline{S_3})} = \frac{\frac{F_{w1}}{V_1}-\frac{F_{w2}}{V_2}}{\frac{F_{w1}}{V_1}-\frac{F_{w3}}{V_3}} = \frac{V_3}{V_2}(\frac{V_2F_{w1}-V_1F_{w2}}{V_3F_{w1}-V_1F_{w3}})$.

Thus, the theoretical solution to the 3S model gives the minimum period of the multicentennial oscillatory mode as follows,

$$T_{min} = \frac{2\pi}{\frac{1}{2}\sqrt{\Delta_{max}}} = \frac{2\pi}{\bar{q}}\frac{1}{\sqrt{\sigma_1\sigma_2}}\frac{1}{\sqrt{1+\frac{\sigma_1}{\sigma_2}M^2-\left(\frac{\sigma_1}{\sigma_2}+1-\frac{\sigma_3}{\sigma_2}\right)M}}$$
$$= \frac{2\pi\sqrt{V_1V_2}}{\bar{q}}\frac{1}{\sqrt{1+\frac{V_2}{V_1}M^2-\left(\frac{V_2}{V_1}-\frac{V_2}{V_3}+1\right)M}} \quad \text{(B11)}$$

In M, $\frac{1}{V_1}(\overline{S_2}-\overline{S_1})$, $\frac{1}{V_2}(\overline{S_3}-\overline{S_2})$, and $\frac{1}{V_3}(\overline{S_1}-\overline{S_3})$ represent the relative contribution of perturbation advection (i.e., $q'(\overline{S_2}-\overline{S_1})$, $q'(\overline{S_3}-\overline{S_2})$, and $q'(\overline{S_1}-\overline{S_3})$) to S_1', S_2', and S_3'. Hence, the physics of M is the relative contribution of perturbation advection to $\frac{S_1'-S_2'}{S_1'-S_3'}$, which is positively correlated with $\frac{-\bar{q}(S_2'-S_1')}{q'(\overline{S_2}-\overline{S_1})}$ and $\frac{-\bar{q}(S_2'-S_1')}{q'(\overline{S_1}-\overline{S_3})}$, the specific values of the negative mean advection and positive perturbation advection feedbacks. This result suggests that when mean advection dominates, stronger negative feedback of mean advection and weaker (stronger) positive perturbation advection feedback shorten the period; when perturbation advection feedback dominates, the same change can lengthen the period.

Mathematically, a damped oscillation in the 3-box model can exist when Re(ω) < 0. Therefore, the stability criterion can be expressed as follows,

$$\lambda < \lambda_C \equiv (\sigma_1+\sigma_2+\sigma_3)\frac{\bar{q}}{M_{sn}-M_s} \quad \text{(B12)}$$

When $\lambda = \lambda_C$, Re(ω) = 0. The period of the undamped oscillation is given by,

$$\Delta_C = -4\left({C_1}^2 + C_2C_3\right) = -4[(\sigma_1+\sigma_2)^2\bar{q}^2 - \sigma_1\bar{q}(M_{sn}-M_{ss})\lambda_C - \sigma_1\sigma_2\bar{q}^2]$$
$$= -4\bar{q}^2[(\sigma_1+\sigma_2)^2 - \sigma_1(\sigma_1+\sigma_2+\sigma_3)M - \sigma_1\sigma_2] \quad \text{(B13a)}$$

$$T_C = \frac{2\pi}{\frac{1}{2}\sqrt{\Delta_C}} = \frac{2\pi}{\bar{q}}\frac{1}{\sqrt{\sigma_1(\sigma_1+\sigma_2+\sigma_3)M+\sigma_1\sigma_2-(\sigma_1+\sigma_2)^2}} \quad \text{(B13b)}$$

There is a relationship between λ_{max}, λ_C and M, that is,

$$\frac{\lambda_{max}}{\lambda_C} = \frac{-(M_{sn}-M_s)(\sigma_1+\sigma_2-\sigma_3)+2\sigma_1(M_{sn}-M_{ss})}{(\sigma_1+\sigma_2+\sigma_3)(M_{sn}-M_s)} = \frac{-(\sigma_1+\sigma_2-\sigma_3)+2\sigma_1M}{\sigma_1+\sigma_2+\sigma_3} \quad \text{(B14)}$$

Therefore, the minimum period and critical period can be written as follows,

$$T_{min} = \frac{2\pi}{\frac{1}{2}\sqrt{\Delta_{max}}} = \frac{2\pi}{\bar{q}}\frac{1}{\sqrt{\sigma_1\sigma_2}}\frac{1}{\sqrt{1-\frac{(\sigma_1+\sigma_2-\sigma_3)^2}{4\sigma_1\sigma_2}+\frac{(\sigma_1+\sigma_2+\sigma_3)^2}{4\sigma_1\sigma_2}\frac{{\lambda_{max}}^2}{{\lambda_C}^2}}}$$

$$= \frac{2\pi\sqrt{V_1V_2}}{\bar{q}}\frac{1}{\sqrt{1-\frac{(V_2V_3+V_1V_3-V_1V_2)^2}{4V_1V_2{V_3}^2}+\frac{(V_2V_3+V_1V_3+V_1V_2)^2}{4V_1V_2{V_3}^2}\frac{{\lambda_{max}}^2}{{\lambda_C}^2}}} \tag{B15a}$$

$$T_C = \frac{2\pi}{\frac{1}{2}\sqrt{\Delta_C}} = \frac{2\pi}{\bar{q}}\frac{1}{\sqrt{\frac{\lambda_{max}}{\lambda_C}\frac{(\sigma_1+\sigma_2+\sigma_3)^2}{2}-\frac{{\sigma_1}^2+{\sigma_2}^2+{\sigma_3}^2}{2}}}$$

$$= \frac{2\pi}{\bar{q}}\frac{1}{\sqrt{\frac{\lambda_{max}}{\lambda_C}\frac{(V_2V_3+V_1V_3+V_1V_2)^2}{2{V_1}^2{V_2}^2{V_3}^2}-\frac{{V_2}^2{V_3}^2+{V_1}^2{V_3}^2+{V_1}^2{V_2}^2}{2{V_1}^2{V_2}^2{V_3}^2}}} \tag{B15b}$$

Eq. (B15) indicates that both the minimum period and critical period depend on basin geometry, mean AMOC strength, and the specific ratio of λ_{max}: λ_C. In the theoretical solution, the ratio has a relationship with M [Eq. (B14)], a function of surface freshwater flux. However, in the real world, the ratio can be more flexible and be affected by other processes of the climate system.

If we let F_{w2} = 0 and F_{w1} + F_{w3} = 0, we will have $\overline{S_2}$ = $\overline{S_3}$ and

$$M = \frac{V_3}{V_1+V_3} \tag{B16a}$$

The theoretical solution of the period becomes,

$$T = \frac{2\pi}{\bar{q}}\sqrt{\frac{V_1V_2}{\frac{V_1V}{(V_1+V_3)^2}}} = \frac{2\pi(V_1+V_3)}{\bar{q}}\sqrt{\frac{V_2}{V_1+V_2+V_3}} \tag{B16b}$$

If we let F_{w3} = 0 and F_{w1} + F_{w2} = 0, we will have $\overline{S_1} = \overline{S_3}$ and

$$M = 1 + \frac{V_1}{V_2} \tag{B17a}$$

The theoretical solution of the period becomes,

$$T = \frac{2\pi}{\bar{q}}\sqrt{\frac{V_1V_2}{\frac{V}{V_3}}} = \frac{2\pi}{\bar{q}}\sqrt{\frac{V_1V_2V_3}{V_1+V_2+V_3}} \tag{B17b}$$

When F_{w3} = 0, we also obtain $\lambda_{max} = \lambda_C$, which may be very similar to the condition in the real world.

Eqs. (B16) and (B17) indicate that when the freshwater flux of the equatorial or South Atlantic ocean is set to zero (i.e., $F_{w2} = 0$ or $F_{w3} = 0$), the solutions of minimum period become unrelated to the surface freshwater flux and depend only on the basin geometry and AMOC strength. This result is consistent with that in LY22 where the freshwater flux in the equatorial ocean is equal to that in the North Atlantic.

REFERENCES

Askjær, T. G., and Coauthors, 2022: Multi-centennial Holocene climate variability in proxy records and transient model simulations. *Quat. Sci. Rev.*, **296,** 107801, https://doi.org/10.1016/j.quascirev.2022.107801.

Bond, G., and Coauthors, 1997: A pervasive millennial-scale cycle in North Atlantic Holocene and glacial climates. *Science*, **278,** 1257-1266, https://doi.org/10.1126/science.278.5341.1257.

Burls, N. J., A. V. Fedorov, D. M. Sigman, S. L. Jaccard, R. Tiedemann, and G. H. Haug, 2017: Active Pacific meridional overturning circulation (PMOC) during the warm Pliocene. *Science Advances*, **3,** e1700156, https://doi.org/10.1126/sciadv.1700156.

Cao, N., Q. Zhang, K. E. Power, F. Schenk, K. Wyser, and H. Yang, 2023: The role of internal feedbacks in sustaining multi-centennial variability of the Atlantic Meridional Overturning Circulation revealed by EC-Earth3-LR simulations. *Earth and Planetary Science Letters*, **621,** 118372.

Dansgaard, W., S. Johnsen, H. Clausen, D. Dahl‐Jensen, N. Gundestrup, C. Hammer, and H. Oeschger, 1984: North Atlantic climatic oscillations revealed by deep Greenland ice cores. *Climate processes and climate sensitivity*, **29,** 288-298.

Delworth, T. L., and F. Zeng, 2012: Multicentennial variability of the Atlantic meridional overturning circulation and its climatic influence in a 4000 year simulation of the GFDL CM2.1 climate model. *Geophys. Res. Lett.*, **39**, https://doi.org/10.1029/2012gl052107.

Döscher, R., and Coauthors, 2022: The EC-Earth3 Earth system model for the Coupled Model Intercomparison Project 6. *Geoscientific Model Development*, **15,** 2973-3020, https://doi.org/10.5194/gmd-15-2973-2022.

Griesel, A., and M. A. M. Maqueda, 2006: The relation of meridional pressure gradients to North Atlantic deep water volume transport in an ocean general circulation model. *Climate Dyn.*, **26,** 781-799, https://doi.org/10.1007/s00382-006-0122-z.

Griffies, S. M., and E. Tziperman, 1995: A linear thermohaline oscillator driven by stochastic atmospheric forcing. *J. Climate*, **8,** 2440-2453, https://doi.org/10.1175/1520-0442(1995)008<2440:ALTODB>2.0.CO;2.

Guan, Y. P., and R. X. Huang, 2008: Stommel's box model of thermohaline circulation revisited—The role of mechanical energy supporting mixing and the wind-driven gyration. *J. Phys. Oceanogr.*, **38,** 909-917, https://doi.org/10.1175/2007JPO3535.1.

Hughes, T. M. C., and A. J. Weaver, 1994: Multiple Equilibria of an Asymmetric Two-Basin Ocean Model. *J. Phys. Oceanogr.*, **24,** 619-637, https://doi.org/10.1175/1520-0485(1994)024<0619:meoaat>2.0.co;2.

Jiang, W., G. Gastineau, and F. Codron, 2021: Multicentennial variability driven by salinity exchanges between the Atlantic and the Arctic Ocean in a coupled climate model. *J. Adv. Model. Earth Syst.*, **13,** e2020MS002366, https://doi.org/10.1029/2020MS002366.

Kamenkovich, I. V., and P. J. Goodman, 2000: The dependence of AABW transport in the Atlantic on vertical diffusivity. *Geophys. Res. Lett.*, **27,** 3739-3742, https://doi.org/10.1029/2000gl011675.

Klockmann, M., U. Mikolajewicz, H. Kleppin, and J. Marotzke, 2020: Coupling of the Subpolar Gyre and the Overturning Circulation During Abrupt Glacial Climate Transitions. *Geophys. Res. Lett.*, **47**, https://doi.org/10.1029/2020gl090361.

Li, Y., and H. Yang, 2022: A Theory for Self-Sustained Multicentennial Oscillation of the Atlantic Meridional Overturning Circulation. *J. Climate*, **35,** 5883-5896, https://doi.org/10.1175/jcli-d-21-0685.1.

Martin, T., W. Park, and M. Latif, 2013: Multi-centennial variability controlled by Southern Ocean convection in the Kiel Climate Model. *Climate Dyn.*, **40,** 2005-2022, https://doi.org/10.1007/s00382-012-1586-7.

——, 2015: Southern Ocean forcing of the North Atlantic at multi-centennial time scales in the Kiel Climate Model. *Deep Sea Res., Part II*, **114,** 39-48, https://doi.org/10.1016/j.dsr2.2014.01.018.

McCreary, J. P., and P. Lu, 1994: Interaction between the subtropical and equatorial ocean circulations: The subtropical cell. *J. Phys. Oceanogr.*, **24,** 466-497.

Meccia, V. L., R. Fuentes-Franco, P. Davini, K. Bellomo, F. Fabiano, S. Yang, and J. Von Hardenberg, 2022: Internal multi-centennial variability of the Atlantic Meridional Overturning Circulation simulated by EC-Earth3. *Climate Dyn.*, https://doi.org/10.1007/s00382-022-06534-4.

Mehling, O., K. Bellomo, M. Angeloni, C. Pasquero, and J. Von Hardenberg, 2023: High-latitude precipitation as a driver of multicentennial variability of the AMOC in a climate model of intermediate complexity. *Climate Dyn.*, **61,** 1519-1534, https://doi.org/10.1007/s00382-022-06640-3.

Moffa‐Sánchez, P., and Coauthors, 2019: Variability in the Northern North Atlantic and Arctic Oceans Across the Last Two Millennia: A Review. *Paleoceanogr. Paleoclimatology.*, **34,** 1399-1436, https://doi.org/10.1029/2018pa003508.

Mysak, L., T. Stocker, and F. Huang, 1993: Century-scale variability in a randomly forced, two-dimensional thermohaline ocean circulation model. *Climate Dyn.*, **8,** 103-116.

Okazaki, Y., A. Timmermann, L. Menviel, N. Harada, A. Abe-Ouchi, M. Chikamoto, A. Mouchet, and H. Asahi, 2010: Deepwater formation in the North Pacific during the last glacial termination. *Science*, **329,** 200-204.

Park, W., and M. Latif, 2008: Multidecadal and multicentennial variability of the meridional overturning circulation. *Geophys. Res. Lett.*, **35**, https://doi.org/10.1029/2008gl035779.

Pasquero, C., and E. Tziperman, 2004: Effects of a Wind-Driven Gyre on Thermohaline Circulation Variability. *J. Phys. Oceanogr.*, **34,** 805-816, https://doi.org/10.1175/1520-0485(2004)034<0805:eoawgo>2.0.co;2.

Prange, M., L. Jonkers, U. Merkel, M. Schulz, and P. Bakker, 2023: A multicentennial mode of North Atlantic climate variability throughout the Last Glacial Maximum. *Science Advances*, **9,** eadh1106.

Rahmstorf, S., 1996: On the freshwater forcing and transport of the Atlantic thermohaline circulation. *Climate Dyn.*, **12,** 799-811, https://doi.org/10.1007/s003820050144.

Rivin, I., and E. Tziperman, 1997: Linear versus Self-Sustained Interdecadal Thermohaline Variability in a Coupled Box Model. *J. Phys. Oceanogr.*, **27,** 1216-1232, https://doi.org/10.1175/1520-0485(1997)027<1216:Lvssit>2.0.Co;2.

Schott, F. A., J. P. McCreary Jr, and G. C. Johnson, 2004: Shallow overturning circulations of the tropical-subtropical oceans. *Washington DC American Geophysical Union Geophysical Monograph Series*, **147,** 261-304.

Scott, J. R., J. Marotzke, and P. H. Stone, 1999: Interhemispheric thermohaline circulation in a coupled box model. *J. Phys. Oceanogr.*, **29,** 351-365, https://doi.org/10.1175/1520-0485(1999)029<0351:ITCIAC>2.0.CO;2.

Sejrup, H. P., H. Haflidason, and J. T. Andrews, 2011: A Holocene North Atlantic SST record and regional climate variability. *Quat. Sci. Rev.*, **30,** 3181-3195, https://doi.org/10.1016/j.quascirev.2011.07.025.

Sévellec, F., T. Huck, and M. Ben Jelloul, 2006: On the mechanism of centennial thermohaline oscillations. *J. Mar. Res.*, **64,** 355-392, https://doi.org/10.1357/002224006778189608.

Smith, R., and Coauthors, 2010: The parallel ocean program (POP) reference manual ocean component of the community climate system model (CCSM) and community earth system model (CESM). *LAUR-01853*, **141,** 1-140.

Srokosz, M., M. Baringer, H. Bryden, S. Cunningham, T. Delworth, S. Lozier, J. Marotzke, and R. Sutton, 2012: Past, Present, and Future Changes in the Atlantic Meridional Overturning Circulation. *Bull. Amer. Meteor. Soc.*, **93,** 1663-1676, https://doi.org/10.1175/bams-d-11-00151.1.

Stocker, T. F., and L. A. Mysak, 1992: Climatic fluctuations on the century time scale: A review of high-resolution proxy data and possible mechanisms. *Clim. Change*, **20,** 227-250, https://doi.org/10.1007/BF00139840.

Sun, J., M. Latif, and W. Park, 2021: Subpolar Gyre – AMOC – Atmosphere Interactions on Multidecadal Timescales in a Version of the Kiel Climate Model. *J. Climate***,** 1-56, https://doi.org/10.1175/jcli-d-20-0725.1.

Swingedouw, D., T. Fichefet, H. Goosse, and M. F. Loutre, 2009: Impact of transient freshwater releases in the Southern Ocean on the AMOC and climate. *Climate Dyn.*, **33,** 365-381, https://doi.org/10.1007/s00382-008-0496-1.

te Raa, L. A., and H. A. Dijkstra, 2003: Modes of internal thermohaline variability in a single-hemispheric ocean basin. *J. Mar. Res.*, **61,** 491-516.

Thorpe, R. B., J. M. Gregory, T. C. Johns, R. A. Wood, and J. F. B. Mitchell, 2001: Mechanisms Determining the Atlantic Thermohaline Circulation Response to Greenhouse Gas Forcing in a Non-Flux-Adjusted Coupled Climate Model. *J. Climate*, **14,** 3102-3116, https://doi.org/10.1175/1520-0442(2001)014<3102:MDTATC>2.0.CO;2.

Treguier, A. M., and Coauthors, 2014: Meridional transport of salt in the global ocean from an eddy-resolving model. *Ocean Sci.*, **10,** 243-255, https://doi.org/10.5194/os-10-243-2014.

Vallis, G. K., and R. Farneti, 2009: Meridional energy transport in the coupled atmosphere-ocean system: scaling and numerical experiments. *Quart. J. Roy. Meteor. Soc.*, **135,** 1643-1660, https://doi.org/10.1002/qj.498.

Wanner, H., and Coauthors, 2008: Mid- to Late Holocene climate change: an overview. *Quat. Sci. Rev.*, **27,** 1791-1828, https://doi.org/10.1016/j.quascirev.2008.06.013.

Weber, S., T. Crowley, and G. Van der Schrier, 2004: Solar irradiance forcing of centennial climate variability during the

Holocene. *Climate Dyn.*, **22,** 539-553, https://doi.org/10.1007/s00382-004-0396-y.

Winton, M., and E. S. Sarachik, 1993: Thermohaline oscillations induced by strong steady salinity forcing of ocean general circulation models.

Wood, R. A., J. M. Rodríguez, R. S. Smith, L. C. Jackson, and E. Hawkins, 2019: Observable, low□order dynamical controls on thresholds of the Atlantic meridional overturning circulation. *Climate Dyn.*, **53,** 6815-6834, https://doi.org/10.1007/s00382-019-04956-1.

Yang, H., Q. Li, K. Wang, Y. Sun, and D. Sun, 2015: Decomposing the meridional heat transport in the climate system. *Climate Dyn.*, **44,** 2751-2768, https://doi.org/10.1007/s00382-014-2380-5.

Yang, K., H. Yang, and Y. Li, 2023: A Theory for Self-sustained Multicentennial Oscillation of the Atlantic Meridional Overturning Circulation. Part II: Role of Temperature. *J. Climate*, https://doi.org/10.1175/JCLI-D-22-0755.1.

Yong-Qi, G., and Y. Lei, 2008: Subpolar Gyre Index and the North Atlantic Meridional Overturning Circulation in a Coupled Climate Model. *Atmos. Ocean. Sci. Lett.*, **1,** 29-32, https://doi.org/10.1080/16742834.2008.11446764.